High order moment model for polydisperse evaporating sprays towards interfacial geometry

Mohamed Essadki, Stephane de Chaisemartin, Frédérique Laurent, Marc Massot

HIGH ORDER MOMENT MODEL FOR POLYDISPERSE EVAPORATING SPRAYS TOWARDS INTERFACIAL GEOMETRY DESCRIPTION*

MOHAMED ESSADKI†, STEPHANE DE CHAISEMARTIN‡, FRÉDÉRIQUE LAURENT§, AND MARC MASSOT¶

Abstract. In this paper we propose a new Eulerian modeling and related accurate and robust numerical methods, describing polydisperse evaporating sprays, based on high order moment methods in size. The main novelty of this model is its capacity to describe some geometrical variables of the droplet-gas interface, by analogy with the liquid-gas interface in interfacial flows [19]. For this purpose, we use fractional size-moments, where the size variable is taken as the droplet surface. In order to evaluate the evaporation of the polydisperse spray, we use a smooth reconstruction which maximizes the Shannon entropy [48]. However, the use of fractional moments introduces some theoretical and numerical difficulties, which need to be tackled. First, relying on a study of the moment space, we extend the Maximum Entropy (ME) reconstruction of the size distribution to the case of fractional moments. Then, we propose a new accurate and realizable algorithm to solve the moment evolution due to evaporation, which preserves the structure of the moment space. This algorithm is based on a mathematical analysis of the kinetic evolution due to evaporation, where it shown that the evolution of some negative order fractional moments have to be properly predicted, a peculiarity related to the use of fractional moments. The present model and numerical schemes yield an accurate and stable evaluation of the moment dynamics with minimal number of variables, as well as a minimal computational cost as with the EMSM model [47, 38], but with the very interesting additional capacity of coupling with diffuse interface model and transport equation of averaged geometrical interface variables, which are essential in oder to describe atomization.

Key words. High order moment method, moment space, realizable high order numerical scheme, polydisperse spray, evaporation, entropy maximization, interface geometry.

AMS subject classifications. 76T10, 35Q35, 65M08, 65M12, 65M99, 65D99.

1. Introduction.

In the last decades, with the large change of the Earth's climate, the increase of energy demand and the high consumption of fossil resources, automotive industries are widely concerned to improve engine efficiency and reduce emissions. Actually, in automotive engines and particularly Diesel engine, the fuel is stored as a liquid phase and injected at high pressure in the combustion chamber. The flow of injected fuel in liquid form mixing with air in the combustion chamber is a complex two-phase flow, which has a direct impact on the combustion regime and pollutant emissions. The difficulties of getting accurate measurements inside an engine and the high cost of experiments [7, 22, 34, 40, 53, 54, 60], make numerical simulations a promising and powerful tool. They aim at providing predictive simulations of the flow in automotive engines and understand the various physical mechanisms involved in this complex problem. The liquid phase is initially separated from the

*This work was funded by a PhD Grant for M. Essadki by IFPEn.

†IFP Energies nouvelles, 1-4 avenue de Bois-Préau, 92852 Rueil-Malmaison Cedex and Laboratoire EM2C, CNRS, CentraleSupélec,Université Paris-Saclay, Grande Voie des Vignes, 92295 Châtenay-Malabry, Cedex - France (mohamed.essadki@centralesupelec.fr).

‡IFP Energies nouvelles, 1-4 avenue de Bois-Préau, 92852 Rueil-Malmaison Cedex - France (stephane.de-chaisemartin@ifpen.fr).

§CNRS, Laboratoire EM2C, CNRS, CentraleSupélec,Université Paris-Saclay, Grande Voie des Vignes, 92295 Châtenay-Malabry, Cedex - France and Fédération de Mathématiques de l'Ecole Centrale Paris, FR CNRS 3487 (frederique.laurent@centralesupelec.fr).

¶Laboratoire EM2C, CNRS, CentraleSupélec,Université Paris-Saclay, Grande Voie des Vignes, 92295 Châtenay-Malabry, Cedex - France and Fédération de Mathématiques de l'Ecole Centrale Paris, FR CNRS 3487 (marc.massot@centralesupelec.fr).

gaseous phase, in the neighborhood of the injector nozzle, we have to deal with what is called a separated phases two-phase flow. The interaction with the surrounding gas leads to a complex interface dynamics and eventually to the atomization of the dense liquid core to a polydisperse evaporating spray, in the downstream region, where evaporation and combustion are taking place.

Modeling the fuel injection flow faces major challenges, because of the multi-scale character of this two-phase flow problem. Indeed, it involves a large scale spectrum, varying from the large scales in the separated phases zone to the small scales in the disperse phase. Direct Numerical Simulations (DNS) have been widely used to solve the full flow dynamics in both phases with a full resolution of the interface. The flow in each phase is modeled through the monophasic Navier-Stokes equation and the interface is determined by using *tracking methods* (Lagrangian methods [33], Marker And Cell (MAC) methods [32]) or by *interface capturing and reconstruction* (VOF, Level-Set and hybrid method - see [49, 46, 9, 23, 1, 13, 58, 59] and references therein). These methods have shown a high accuracy in predicting a sharp interface for incompressible and compressible flows. But, they require a high mesh resolution to compute the solution and they fail to capture the full range of droplet sizes in realistic configuration of high Reynolds and Weber numbers. Therefore, reduced-order models, where averaging approaches are envisioned, have to be considered since a full resolution is out of reach for industrial applications.

The actual existing reduced-order models are not suitable to simulate the whole process of the fuel injection. Instead, two reduced-order model classes have been used depending on the flow region. In the dense core region, diffuse interface models can be used to simulate the flow with lower computational cost. In these models, the interface is considered as a mixing zone, such that the two phases coexist at the same macroscopic position, where each phase occupies a portion of the volume. Several strategies and equilibrium level can be used in order to derive such equations either following an averaging process [18], using fluid mechanics and thermodynamics of irreversible processes [2] or using the principle of least action [21] (see also [45, 44] and references therein). At the interface, the artificial fluid mixing leads to some level of diffusion of the interface, and as a consequence, we lose important information about the interface geometry. Indeed, the volume fraction is the only variable used to describe the interface geometry, whereas the details of the atomization process cannot be predicted so far with such averaged models. To gain more precision in capturing the atomization, some models add a transport equation of the interface area density [62, 35, 46]. However, two variables (volume fraction and interface area density) are not sufficient to describe the polydispersion in the disperse phase region.

In this region of the disperse phase, the dynamics and evaporation of droplets are conditioned by their size. Consequently, size distribution effects should be described in any attempt of modeling a polydisperse spray. The second reduced-order model class relies on a kinetic approach, which has been widely used to describe accurately a population of particle at mesoscopic level and has been shown to be efficient in a number of cases. In this approach, a cloud of droplets is modeled by a number density function (NDF), which satisfies a generalized population balance equation (GPBE), also called Williams-Boltzmann (WBE) equation [65]. The internal variables of the NDF provide a statistical description of some relevant physical properties such as the droplet size, velocity and temperature. The numerical resolution of WBE can be

achieved by the Lagrangian Monte-Carlo approach [3]. This method is considered to be the most accurate for solving WBE, but leads to a high computational cost for unsteady flows and requires complex load-balancing algorithms in parallel computation. Finally, we encounter some difficulties to couple this Lagrangian method for the dynamics of the spray with an Eulerian method used to solve the continuous phase. Alternative method consists in deriving an Eulerian moment model from the WBE. In this approach, a differential system of a finite set of moments of the NDF is closed through some closure assumptions on the velocity and size distributions, as long as the considered phase space variables are the velocity and the size. The unclosed velocity moment terms are closed by expressing the NDF as a function of the known velocity moments [38, 4, 5, 63] (monokinetic, Maxwell-Boltzmann, anisotropic Gaussian closures, ...). For the modeling of the size distribution, three possible approaches can be used: 1-The first one consists in discretizing the size direction into sections and to use low order size moments in each of these sections. This approach is commonly known as Multi-fluid models [30, 41, 43]. 2- The second one provides a closure of negative as well as fractional moments from the integer ones through a logarithm Lagrangian interpolation and is called the MOMIC method [27, 26]; it has been essentially use for soot modeling and simulation. However, such an approach suffers from several issues; as Mueller et al [50] have pointed that it has a hard time dealing with the boundary of the moment space, that is bimodal distributions as observed in experimental measurements [67]. Besides, the interpolation procedure can not preserve the moment space in general and can suffer from important inaccuracy due to the way the negative order moments are approximated. 3- The third approach involves high order moments using either a quadrature of the distribution or a smooth reconstruction using a sum of kernel density functions and quadrature [51, 66] or Entropy maximization [38, 24, 47] on the whole size range. The Multi-fluid model suffers from numerical diffusion in the size direction, especially when we are dealing with evaporation, while high order moment approach do not encounter this limitation, instead it requires to solve complex algebra by using high order moments. Furthermore, the computation of the flux of the disappearance droplet through evaporation requires a pointwise evaluation of the size distribution at zero size, which leads to a singular flux in the case of quadrature closure (such as QMOM or DQMOM approaches). On the other hand, the continuous reconstruction through Entropy maximization, used the first time in the EMSM [38, 47] and CSVM [64] models, shows a great capacity in modeling the polydispersion and evaluating precisely the evaporation fluxes, with a minimal number of variables. Indeed, high order moments make polydisperse modeling possible with only one size-section. Eventually, we can also use an hybrid approach, where we couple high order moment model with the multi-fluid approach. In that case, few sections can be used to gain more accuracy in simulating the droplet dynamics [64].

So far, the existing models do not provide a unified description of the two regions of the flows (separated and disperse phases). In the present contribution, we propose a new high order moment model for the disperse phase with the capacity of describing the interface geometry by analogy with interfacial flows [19]. Our strategy is to resolve the polydispersion by using a set of variables, which can be identified as averages of the gas-liquid interface geometry. For this purpose, we show that some geometrical variables, which can give an accurate description of a complex interface, can be expressed as fractional size-moments of NDF in the disperse zone, when the size variable is given by the surface of the droplets. The present contribution aims at introducing the mathematics fundamentals of the model and showing that we can

preserve all the advantages of the previously introduced high order moment methods in [38, 47] in terms of accuracy, realizability and robustness, but with a much higher potential in terms of coupling with a diffuse interface model. In fact, to evaluate the evaporation flux, we use the Maximum Entropy reconstruction as it was done in the EMSM model, but this time with fractional moments. Entropy maximization with fractional moments was used in another context [52, 31] as a remedy to the ill-conditioning of the procedure when considering a high number of integer moments [61]. The considered set of fractional moments is then recovered from the integer ones, and their orders are optimized to minimize the entropy difference with the real function. In the present contribution, a known and small set of fractional moments is used, deduced from physical considerations, in such a way that the problematic is different. The existence and uniqueness of this convex optimization problem under constraints is given in [48] in the case of integer moment. While some elements of proof are to be found in the fractional moment case in [39], in the present contribution, we propose a generalization of the result in the case of a special set of fractional moments. Moreover, we need to generalize some useful properties of the fractional moment space such as canonical moment as well as lower principal representation [14]. These properties are relevant elements to design realizable schemes and algorithms to solve a high order moment system i.e. numerical scheme, which preserves the moment vector inside the moment space and yields accuracy and robustness of the numerical strategy. Finally, we propose a new realizable algorithm to solve the evolution of fractional moments due to the evaporation. The resolution of the evaporation is done by evaluating the disappearance flux, then we compute the internal size evolution by using a specific quadrature, which involves negative order of moments and requires an original strategy compared to the integer moment problem. The proposed strategy is then assessed by a careful investigation of the numerical errors as well as a detailed comparison with the original approach in 0D, 1D and 2D academic configurations. A companion paper [25] aims at implementing the proposed model into a massively parallel code with adaptive mesh refinement and showing the potential of the model and numerical method towards realistic engine simulations.

The paper is organized as follows. In a second section, the two-phase flow modeling of polydisperse evaporating sprays in a carrier gaseous flow field as well as the original high order moment modeling are introduced; we also recall the classical averaged geometrical description of interfacial flows in order to identify the relevant geometrical averaged variables. Section 3 is then devoted to the introduction of the new geometrical high order moments for a polydisperse spray as well as the resulting system of partial differential equations on moments derived from the WBE. The closure of the system through maximization of entropy is then presented and its mathematical properties detailed. Once the proposed system of equations is closed, Section 4 and 5 are dedicated to the numerical resolution of the obtained system. While Section 4 is devoted to the transport in phase space, Section 5 focuses on the transport in physical space. Section 6 is eventually concerned with the numerical verification and results in 0D, 1D and 2D, thus assessing the proposed modeling and numerical strategy, before concluding.

2. Two phase flows modeling.

2.1. Kinetic modeling of polydisperse spray. The spray consists in a cloud of polydisperse droplets, which can be described statistically with the number density function (NDF) $f^{\phi}(t, \boldsymbol{x}, \boldsymbol{c}, \phi, T)$. This function represents the probable number of

droplets located at position $\boldsymbol{x}$, travelling with velocity $\boldsymbol{c}$ and having temperature T and size ϕ. In general, the size ϕ of a spherical droplet can be given by its volume V, its surface S or its radius R of the droplet. By considering a spherical form, these three geometrical variables are equivalent $f^V dV = f^S dS = f^R dR$. In the following, we use the surface S as the size variable. The NDF will be simply noted by f. This function satisfies the Williams-Boltzmann Equation (WBE) [65]:

$$\partial_t f + \partial_{\boldsymbol{x}} \cdot (\boldsymbol{c} f) + \partial_{\boldsymbol{c}} \cdot (\boldsymbol{F} f) + \partial_S \left(\mathrm{R}_S f\right) + \partial_T \left(Q f\right) = \Gamma_c, \tag{1}$$

where $\boldsymbol{F}$ is the acceleration, R_S, the evaporation rate, Q, the thermal transfer and Γ_c, the source term, which includes collisions, secondary breakup and coalescence.

The WBE (1) gives a complete description of the spray dynamics in a general framework. However, the interaction terms (evaporation, acceleration, thermal transfer) with the gaseous phase and the source terms need to be modeled to close the WBE at the kinetic or mesoscopic level. The second step of modeling consists in reducing the large phase space dimension of this equation by using a moment method. Hence, some closures of the NDF have to be used and the set of assumptions clarified. For the sake of simplicity and the clarity of the presentation, we propose to work with a simplified WBE. We consider a dilute spray at high Knudsen number and small and spherical droplets at low Weber number, obtained after the atomization. Under these assumptions, secondary breakup, coalescence and collision can be neglected. We also assume that thermal transfer can be neglected and will mainly focus on one-way coupling. We refer the readers to the following articles and references therein, showing that such a mesoscopic approach is capable of describing coalescence [16], break-up [15], heat transfer [42] and two-way coupling [23, 24]. Furthermore, we consider that the drag force, due to the slip between the droplet and gas velocities, is the only force acting on the droplets. In the following, we model this force by the Stokes law:

$$\boldsymbol{F} = \frac{\boldsymbol{U}_g - \boldsymbol{c}}{\tau_p(S)}, \tag{2}$$

where $\boldsymbol{U}_g$ is the gas velocity and $\tau_p(S)$ is the characteristic response time of the droplet. Finally, we use the d^2 law for evaporation:

$$\mathrm{R}_S(S) = -\mathrm{K}, \tag{3}$$

where K is the constant rate of evaporation.

The modeling and numerical strategy will be presented by considering these simplified assumptions. However, in Appendix A, we discuss how to extend the proposed model and the numerical strategy to a general modeling level.

Considering these assumptions and by using non-dimensional variables, the dimensionless WBE reads:

$$\partial_{t^*} f^* + \partial_{\boldsymbol{x}^*} \cdot (\boldsymbol{c}^* f^*) + \partial_{\boldsymbol{c}^*} \cdot \left(\frac{{\boldsymbol{U}_g}^* - \boldsymbol{c}^*}{\mathrm{St}(S^*)} f^* \right) + \partial_{S^*} (\mathrm{K}^* f^*) = 0, \tag{4}$$

where the superscript $*$ refers to dimensionless variables, and are defined as follows: if the concerned variable is X, we note by X^o the characteristic value of X, then $X^* = X/X^o$. The maximum size $S^o = S_{max}$ will be taken as the characteristic size, thus $S^* \in [0, 1]$, and the characteristic gas time $t^o = \tau_g$ as the characteristic time of

the flow. The Stokes number $\mathrm{St} = \frac{\tau_p(S)}{\tau_g}$ depends linearly on the droplet size :

$$\mathrm{St}(S^*) = \theta S^*, \quad \text{where } \theta = \frac{\rho_l S_{max}}{18\pi\mu_g\tau_g}, \tag{5}$$

where ρ_l is the liquid mass density and μ_g is the gas dynamic viscosity. In the following, we consider only dimensionless variables and we omit the superscript $*$.

2.2. High order size-moment modeling: related closure and moment space. The high dimension nature of the phase space of the WBE makes its discretization not convenient for complex industrial applications. Since the exact resolution of the NDF is not required and only macroscopic quantities of the flows are needed for such applications, an Eulerian moment method can be used to reduce the complexity of WBE. The size-velocity moments of the NDF are expressed as follows:

$$M_{i,j,k,l} = \int_0^1 \int_{\mathbb{R}^3} S^l c_x^i c_y^j c_z^k f(t,\boldsymbol{x},\boldsymbol{c},S)\mathrm{d}S\mathrm{d}^3\boldsymbol{c}. \tag{6}$$

From the WBE, one can derive a system of equation of finite set of these moments. The obtained system is unclosed without any assumption on the NDF form. In the following, we consider that the velocity distribution has a prescribed form:

$$f(t,\boldsymbol{x},\boldsymbol{c},S) = n(t,\boldsymbol{x},S)\varphi(\boldsymbol{c}-\boldsymbol{U}(t,\boldsymbol{x},S)), \quad \text{where} \quad \int_{\mathbb{R}^3}\varphi(\boldsymbol{c})\mathrm{d}^3\boldsymbol{c} = 1, \tag{7}$$

and φ does not depend on droplet size. The closure of the velocity distribution requires a specific treatment, especially when we are concerned with modeling particle trajectory crossing (PTC) at high Knudsen numbers. In such case, the collision operator has a very limited effect on the NDF and does not produce any kind of hydrodynamic equilibrium. For accurate modeling of PTC, one can use high order velocity-moment closed through an anisotropic Gaussian velocity-distribution [63, 55]. In the present work, we are not concerned with these modeling issues, and we will consider a monokinetic velocity distribution, which can be also analyzed as an hydrodynamic equilibrium distribution of Maxwell-Boltzmann type at zero temperature [10]:

$$f(t,\boldsymbol{x},\boldsymbol{c},S) = n(t,\boldsymbol{x},S)\delta(\boldsymbol{c}-\boldsymbol{U}(t,\boldsymbol{x})). \tag{8}$$

This closure does not take into account PTC, since only one velocity is defined per position and time. This assumption is valid for low inertia droplets, when the droplet velocities are rapidly relaxed to the local gas velocity. Thus, the droplets do not experience any crossing. It has been shown in [11] that for an evolving spray of initial distribution of the form (8) and when the Stokes number is lower than the critical value $\mathrm{St}_c =$, the monokinetic assumption is valid all the time. Nevertheless, the model can still be used in the limit of moderately inertial droplets $\mathrm{St} \approx 1$, provided that we use appropriate numerical schemes to handle eventual delta-shocks creation when PTC occurs [10, 38, 55]. Considering this simplified velocity distribution, we derive the following semi-kinetic system from equation (4) by considering moments of order 0 and 1 in velocity:

$$\begin{aligned} \partial_t n + \partial_{\boldsymbol{x}}\cdot(n\boldsymbol{U}) &= K\partial_S n, \\ \partial_t n + \partial_{\boldsymbol{x}}\cdot(n\boldsymbol{U}\otimes\boldsymbol{U}) &= K\partial_S(n\boldsymbol{U}) + n\frac{\boldsymbol{U}_g-\boldsymbol{U}}{\mathrm{St}(S)}. \end{aligned} \tag{9}$$

In the present contribution, we adopt the high order size-moment method with a continuous reconstruction of the size distribution to model a polydisperse spray. This approach, based mainly on [47, 36, 38, 37], consists in deriving a dynamical system of finite set of size-moments of the NDF. The integer size-moments are defined as follows, with $N \geq 1$ for a non dimensional size interval $[0, 1]$:

$$\mathbf{m} = \begin{pmatrix} \mathrm{m}_0 \\ \vdots \\ \mathrm{m}_N \end{pmatrix}, \quad \mathrm{m}_k = \int_0^1 S^k n(t, \boldsymbol{x}, S) dS. \tag{10}$$

The system of the EMSM model obtained from an integration of the semi-kinetic system (9) over $S \in [0, 1]$ multiplied by S^k:

$$\begin{array}{rcll} \partial_t \mathrm{m}_0 + \partial_{\boldsymbol{x}}.(\mathrm{m}_0 \boldsymbol{U}) & = & -\mathrm{K} n(t, \boldsymbol{x}, S = 0) & , \\ \partial_t \mathrm{m}_1 + \partial_{\boldsymbol{x}}.(\mathrm{m}_1 \boldsymbol{U}) & = & -\mathrm{K}\ \mathrm{m}_0 & , \\ \vdots & & \vdots & \\ \partial_t \mathrm{m}_N + \partial_{\boldsymbol{x}}.(\mathrm{m}_N \boldsymbol{U}) & = & -N\mathrm{K}\ \mathrm{m}_{N-1} & , \\ \partial_t (\mathrm{m}_1 \boldsymbol{U}) + \partial_{\boldsymbol{x}}.(\mathrm{m}_1 \boldsymbol{U} \otimes \boldsymbol{U}) & = & -\mathrm{K}\ \mathrm{m}_0 \boldsymbol{U} & +\mathrm{m}_0 \dfrac{\boldsymbol{U}_g - \boldsymbol{U}}{\theta}. \end{array} \tag{11}$$

Let us remark that, the term $-\mathrm{K} n(t, \boldsymbol{x}, S = 0)$ expresses the pointwise disappearance flux of droplets through evaporation. This term only appears in the first equation. But, it participates in the other moments evolution in the same way through the coupling terms $-k\mathrm{K}\mathrm{m}_{k-1}$, when we consider the integral formulation of this system [47]. To close the system, we need to determine the size distribution from the known moments.

Before proposing a closure of this model, let us recall the definition of the moment space and some useful properties. We denote by $P([0, 1])$ the set of all probability density measures of the interval $[0, 1]$. Then the Nth "normalized" moment space $\mathbb{M}_N$ is define as follows:

$$\mathbb{M}_N = \{\boldsymbol{c}_N(\mu), \mu \in P\}, \quad \boldsymbol{c}_N = (c_0(\mu), \ldots, c_N(\mu)), \quad c_k(\mu) = \int_0^1 x^k \mu(x) dx \tag{12}$$

Let us notice that $c_0 = 1$, since we use probability density measures in this definition. In our case, we can normalize by m_0 to associate the moment vector $(\mathrm{m}_0, \ldots, \mathrm{m}_N)^t$ to $(c_0, \ldots, c_N)^t \in \mathbb{M}_N$, where $c_k = \mathrm{m}_k / \mathrm{m}_0$. The Nth "normalized" moment space is a convex and bounded space.

Definition 1. *We define the Nth moment space, the set of vectors* $(\mathrm{m}_0, \ldots \mathrm{m}_N)^t$*, whose normalized vector by the number density* m_0 *belongs to the* N^{th} *normalized moment space.*

Considering this definition and some results from [14]: if $(\mathrm{m}_0, \ldots, \mathrm{m}_N)^t$ is in the interior of the moment space, there exists an infinity of size distributions, which represent this moment vector. In other word, there exists an infinity of size distributions $n(S)$, which are the solution of the following finite Hausdroff problem:

$$\mathrm{m}_k = \int_0^1 S^k n(S) dS, \quad k = 0 \ldots N. \tag{13}$$

Massot et al [47] proposed to use a continuous reconstruction of the size distribution through the maximization of Shannon entropy:

$$H(n) = -\int_0^1 n(S) ln(n(S)) dS. \tag{14}$$

The existence and uniqueness of a size distribution $n^{ME}(S)$ which maximizes the Shannon entropy and is the solution of the finite Hausdroff moment problem (13) was proved in [48] for the moment of integer order, when the moment vector belongs to the interior of the moment space and the solution is shown to have the following form:

$$n(S) = \exp\left(-(\lambda_0 + \lambda_1 S + \ldots + \lambda_N S^N)\right), \tag{15}$$

where coefficients λ_k, are determined from system (13). In the same article, the authors propose an algorithm to solve this constrained optimization problem, based on Newton-Raphson method. A discussion of the limitation of this algorithm when the moment vector is close to the boundary of the moment space, or equivalently when the ME reconstructed size-distribution approaches to a sum of delta Dirac functions, is given in [47]. Vié et al [64] proposed some more advanced solutions to cope with this problem, by tabulating the coefficients depending on the moments and by using an adaptive support for the integral calculation, which enables an accurate computation of the integral moments when the NDFs are nearly singular.

This approach shows a high capacity in describing the dynamic of a polydisperse spray using only one size-section. Even though the high order moment formalism provides some key information about polydispersion, it is important to realize that it is restricted to the disperse phase zone. Coupling such an approach with a separated phases model requires some complementary information, which the usual approaches of diffuse interface models can not provide. Indeed, diffuse interface models, used to simulate a separated phases zone, consider the interface as a continuous band layer, where we have lost important information about the interface geometry. The first step, would be to enrich the diffuse interface models as in [21] in order to transport averaged geometrical variables to gain accuracy about the interface geometry. Nevertheless, even if the usual diffuse interface models would have some more information about the interfacial flow geometry, the coupling of two very different models is usually a rather cumbersome task and relies on some parameters, the described physics will depend on. Consequently we adopt a rather original strategy and we will build a model for the disperse phase, which involves variables that are describing the interface geometry in average, so that we end up with a set of variables that are common to the two zones and can potentially help in building a single unified model able to capture the proper physics in both zones.

In this way, our strategy consists in using averaged geometrical variables in the separated phases zone to model the atomization in future work, and to use the same variables in the disperse phase to describe the atomization by using the same concept as in the EMSM model. However, the integer moments used in the EMSM model do not all represent physical quantities of the flow and more precisely, these moments do not provide information about the interface geometry. Therefore, we need to use other geometrical variables in the disperse phase, while maintaining the attractiveness as well as the efficiency of the EMSM approach. In order to do so, let us introduce the natural geometrical variables in the separated phases zone, before extending this description to the disperse phase.

2.3. Geometrical description of interfacial flows. In many two-phase flow applications, the exact location of each phase is difficult to determine precisely because of the different unpredictable phenomena such as turbulence, interface instabilities and other small scale phenomena that cannot be simulated even with the most powerful supercomputers. Fortunately, in industrial applications, we are more concerned with the averaged features than to the small details of the flow. Therefore, we can use Diffuse Interface Models (DIM) [2, 57, 56, 44] to describe the interface location in terms of probability and averaged quantities based on averaged operators (ensemble averaged, time averaged or volume averaged). In the following, we define some averaged geometrical variables, which can be used to model the interface in separated phases for a complementary geometrical description. Their definitions are based here on the volume averaged operator following the derivation of Drew [19]. First, we define the phase function $\chi_k(t,\boldsymbol{x})$ for a given phase k by:

$$\chi_k(t,\boldsymbol{x}) = \begin{cases} 1, & \text{if } \boldsymbol{x} \in k \\ 0, & \text{otherwise} \end{cases}$$

then, the volume-averaged operator is defined by:

$$\overline{(\bullet)}(t,\boldsymbol{x}) = \frac{1}{|V|}\int_V (\bullet)\chi_k(t,\boldsymbol{x}')dV(\boldsymbol{x}'), \tag{16}$$

where $V \in \mathbb{R}^3$ is a macroscopic space around the position $\boldsymbol{x}$, and $|V|$ is the occupied volume.

Let us emphasize that the DIM can be obtained by applying this operator to the monophasic Navier-Stokes equation. The obtained equations involve the volume fraction variable, which expresses the portion of the occupied volume by a given phase. Moreover, the volume fraction allows to locate the interface up to the averaging scale and is then a first piece of information about the interface geometry:

$$\alpha_k(t,\boldsymbol{x}) = \frac{1}{|V|}\int_V \chi_k(t,\boldsymbol{x}')dV(\boldsymbol{x}'). \tag{17}$$

The second variable treated by Drew [19] and used also in other two-phase flow models [62, 35, 46] is the interfacial area density. The importance of this variable relies mainly on the modeling of exchange terms (evaporation, thermal transfer and drag force) as well as modeling the primary atomization. The interfacial area density is interpreted as the ratio of the surface area of an interface contained in a macroscopic volume and this volume.

$$\Sigma(t,\boldsymbol{x}) = \frac{1}{|V|}\int_V ||\boldsymbol{\nabla}\chi_k(t,\boldsymbol{x}')||dV(\boldsymbol{x}'). \tag{18}$$

So far, the interface modeling is still incomplete, since no information on the interface shape is being given. In fact, the small details of the interface can not be modeled accurately using only two geometrical variables. Drew proposed to introduce the two curvatures of the interface in his model. Indeed, these variables give a complementary description of the interface and are highly related to the atomization process, since they are involved in the jump relations at the interface.

The two local curvatures can be defined as follows: let P be a point of the interface and $\boldsymbol{n}$ is the normal vector at the point P. Then, we take a plane that contains P and parallel to $\boldsymbol{n}$. As the plane rotates around the normal vector, the intersection curve between the interface and the plane defines a curvature at point P which corresponds to the curvature of this 2D curve. As the plane completes a full π rotation, it can be shown that it has reached exactly two extremal curvature values: the two principal curvatures k_1 and k_2.

Drew derived the dynamical equations of the mean and Gauss curvature respectively H and G from the differential definitions of k_1 and k_2. These two variables read:

$$\begin{aligned} \mathrm{H} &= \tfrac{1}{2}(\mathrm{k}_1 + \mathrm{k}_2), \\ \mathrm{G} &= \mathrm{k}_1\mathrm{k}_2. \end{aligned} \tag{19}$$

These variables are defined only at the interface. Therefore, we need a specific averaging for these interfacial variables. So, we introduce the interfacial averaging operator $\widetilde{(\bullet)}$, defined as follows:

$$\Sigma\ \widetilde{(\bullet)}(t,\boldsymbol{x}) = \frac{1}{|V|}\int_V (\bullet)||\boldsymbol{\nabla}\chi_k(t,\boldsymbol{x}')||dV(\boldsymbol{x}'). \tag{20}$$

The interfacial averaged Gauss and mean curvature weighted by the interface are defined as follows :

$$\begin{aligned} \Sigma\widetilde{\mathrm{H}} &= \textstyle\int_V \mathrm{H}||\boldsymbol{\nabla}\chi_k(t,\boldsymbol{x}')||dV(\boldsymbol{x}'), \\ \Sigma\widetilde{\mathrm{G}} &= \textstyle\int_V \mathrm{G}||\boldsymbol{\nabla}\chi_k(t,\boldsymbol{x}')||dV(\boldsymbol{x}'). \end{aligned} \tag{21}$$

These four geometrical variables can be transported and coupled with a diffuse interface model to gain the accuracy on the interface. Drew [19] derived conservative equations for these variables with source terms, which describe the stretch and the wrinkling of the interface. Its derivation is based on a cinematic evolution of an interface, when the interface velocity is given. But in real application, the interface velocity should be determined from the diffuse interface model. In the following, we would like to express these geometrical variables in the disperse phase as size-moments of the size distribution, and derive a new high order moment model using such variables.

3. Geometrical high order moment model.

3.1. Interfacial geometrical variables for the disperse phase. Let us consider a population of spherical droplets represented by their size distribution $n(t,\boldsymbol{x},S)$. Then, by analogy with the separated phases, we express the averaged geometrical variables: volume fraction, interface area density, Gauss curvature and mean curvature in the disperse phase. The definition of these geometrical variables was based on the phase function χ_k. This function contains all the microscopic information about the interface. In the disperse phase, we use the statistical information about the droplet distribution, which is given by the size distribution $n(t,\boldsymbol{x},S)$. Considering this function, we define the different geometrical variables in the context of a polydisperse spray as follows:

A. The *volume fraction* α_d is the sum of the volume of each droplet divided by the contained volume at a given position:

$$\alpha_d = \int_0^1 V(S)n(t,\boldsymbol{x},S)dS. \tag{22}$$

The droplet being spherical, $V(S) = \dfrac{S^{3/2}}{6\sqrt{\pi}}$.

B. The *interfacial area density* Σ_d is the sum of the surface of each droplet divided by the contained volume at a given position:

$$\Sigma_d = \int_0^1 S n(t,\boldsymbol{x},S)dS. \tag{23}$$

C. The two local curvatures are equal for a spherical droplet $\mathrm{k}_1 = \mathrm{k}_2 = \frac{2\sqrt{\pi}}{\sqrt{S}}$. But since we use the mean and Gauss curvatures, we can define two different averaged quantities. Let us notice that, in the case of separated phases, the *average mean and Gauss curvatures* were defined as an average over a volume and weighed by the interfacial area. In the disperse phase case, this becomes:

$$\begin{array}{rcl} \Sigma_d \widetilde{\mathrm{H}}_d &=& \int_0^1 \mathrm{H}(S) S n(t,\boldsymbol{x},S)dS, \\ \Sigma_d \widetilde{\mathrm{G}}_d &=& \int_0^1 \mathrm{G}(S) S n(t,\boldsymbol{x},S)dS. \end{array} \tag{24}$$

These four geometrical variables are expressed as fractional moments of the size distribution $\mathrm{m}_{k/2} = \int_0^1 S^{k/2} n(S)dS$:

$$\begin{array}{rcl} \Sigma_d \widetilde{\mathrm{G}}_d &=& 4\pi \mathrm{m}_0, \\ \Sigma_d \widetilde{\mathrm{H}}_d &=& 2\sqrt{\pi}\mathrm{m}_{1/2}, \\ \Sigma_d &=& \mathrm{m}_1, \\ \alpha_d &=& \frac{1}{6\sqrt{\pi}}\mathrm{m}_{3/2}. \end{array} \tag{25}$$

These moments can be expressed as integer moment by simple variable substitution $x = \sqrt{S}$. However, we prefer to hold the droplet surface as the size variable, since we consider a d^2 evaporation law, where the evaporation rate R_S is constant.

3.2. The governing moment equation. In this section, we derive from the kinetic equation (4) a high order fractional moment model. This model gives the evolution of the mean geometrical interfacial variables due to transport, evaporation and drag force.

$$\left\{ \begin{array}{llcll} \partial_t \mathrm{m}_0 + & \partial_{\boldsymbol{x}} \cdot (\mathrm{m}_0 \boldsymbol{U}) & = & -\mathrm{K} n(t,\boldsymbol{x},S=0), & \\ \partial_t \mathrm{m}_{1/2} + & \partial_{\boldsymbol{x}} \cdot \left(\mathrm{m}_{1/2} \boldsymbol{U}\right) & = & -\dfrac{\mathrm{K}}{2}\mathrm{m}_{-1/2}, & \\ \partial_t \mathrm{m}_1 + & \partial_{\boldsymbol{x}} \cdot (\mathrm{m}_1 \boldsymbol{U}) & = & -\mathrm{K}\mathrm{m}_0, & \\ \partial_t \mathrm{m}_{3/2} + & \partial_{\boldsymbol{x}} \cdot \left(\mathrm{m}_{3/2} \boldsymbol{U}\right) & = & -\dfrac{3\mathrm{K}}{2}\mathrm{m}_{1/2}, & \\ \partial_t \left(\mathrm{m}_1 \boldsymbol{U}\right) + & \partial_{\boldsymbol{x}} \cdot (\mathrm{m}_1 \boldsymbol{U} \otimes \boldsymbol{U}) & = & -\mathrm{K}\mathrm{m}_0 \boldsymbol{U} + & \mathrm{m}_0 \dfrac{\boldsymbol{U}_g - \boldsymbol{U}}{\theta}, \end{array} \right. \tag{26}$$

where $-\mathrm{K}n(t,\boldsymbol{x},S=0)$ represents the pointwise disappearance flux, and the moment of negative order, $\mathrm{m}^{(i)}_{-1/2} = \int_{S_{i-1}}^{S_i} S^{-1/2} n(t,S)dS$, naturally appears in the system after integrating by part the evaporation term in the WBE. In the following, these terms and the associated instantaneous fluxes will be closed by a smooth reconstruction of the size distribution through entropy maximisation.

The use of fractional moment introduces a new mathematical framework of modeling as well as some numerical difficulties, which require a specific treatment. Some useful mathematical properties of the fractional moments space are discussed in Appendix B. These results will be used to design realizable numerical schemes, i.e. schemes that ensure the preservation of the moment vector in the moment space.

3.3. Maximum Entropy reconstruction. NDF reconstruction through the maximum entropy provides a smooth reconstruction to close the moment system (26) as it was done in the EMSM model. The ME reconstruction consists in maximizing the following Shannon entropy:

$$H[n] = -\int_0^1 n(s) ln(n(s)) ds, \tag{27}$$

under the condition that its first $N+1$ (in our case $N=3$) moments are equal to the computed moments

$$\mathrm{m}_{k/2} = \int_0^1 S^{k/2} n(S) dS, \quad k = 0 \dots N. \tag{28}$$

3.3.1. Existence and uniqueness of the solution. In this part, we give a proof of the existence and uniqueness of the ME distribution function. We mention that the case of the integer moments has been already treated in [48]. We have used some ideas of this work. But the present proof is completely different and simplified. Indeed, Mead et al [48] have used the monotonic properties of the moments, which is a characterisation of the integer moment space, to prove existence of the ME solution. In our case, we will only used the definition of the fractional moment space. The ME problem reads:

$$\begin{cases} \max \left\{ H[n] = -\displaystyle\int_0^1 n(S) ln(n(S)) dS \right\}, \\ \mathrm{m}_{k/2} = \displaystyle\int_0^1 S^{k/2} n(S) dS \quad k = 0 \dots N, \end{cases} \tag{29}$$

where $\mathbf{m}_N = (\mathrm{m}_0, \mathrm{m}_{1/2}, .., \mathrm{m}_{N/2})$ is a moment vector in the interior of the fractional moment space $\mathbb{M}_N^{1/2}([0,1])$ (see Appendix B).

LEMMA 2. *If the constrained optimization (29) problem admits a solution, then this solution is unique and can be written in the following form:*

$$n^{ME}(S) = \exp(-\lambda_0 - \sum_{i=1}^{N} \lambda_i S^{i/2}), \tag{30}$$

where $\boldsymbol{\lambda} = (\lambda_0, .., \lambda_N)^t \in \mathbb{R}^N$.

Proof. The Lagrangian function associated to this standard constrained optimization problem is:

$$L(n, \boldsymbol{\lambda}) = H[n] - (\lambda_0 - 1) \left(\int_0^1 n(s) ds - \mathrm{m}_0 \right) - \sum_{i=1}^{N} \left[\lambda_i \left(\int_0^1 s^{i/2} n(s) ds - \mathrm{m}_{i/2} \right) \right], \tag{31}$$

where $\boldsymbol{\lambda} = (\lambda_0, .., \lambda_N)$ is the vector of the Lagrange's multipliers.
Let us suppose that, for a given moment vector $\mathbf{m}_N$, there exists a density function n^{ME} which is the solution of the ME problem (29). So, there exists a vector $\boldsymbol{\lambda}^{ME}$ for which the differential of the Lagrange function $L(n, \boldsymbol{\lambda})$ at the point $(n^{ME}, \boldsymbol{\lambda}^{ME})$ vanishes:

$$\left\{ \begin{array}{rcl} DL(n^{ME}, \boldsymbol{\lambda}) \cdot (h, \mathbf{0}) & = & \int_0^1 h(s) \left[-ln(n^{ME}(s)) - \sum_{i=0}^{N} \lambda_i s^{i/2} \right] ds = 0, \\ \frac{\partial L}{\partial \lambda_i}(n^{ME}, \boldsymbol{\lambda}) & = & \int_0^1 s^{i/2} n^{ME}(s) ds - \mathrm{m}_{i/2} = 0, \end{array} \right. \tag{32}$$

where h is a positive distribution. Since the system (32) is valid for all h, it yields:

$$\left\{ \begin{array}{rcl} n^{ME}(S) & = & \exp(-\lambda_0 - \sum_{i=1}^{N} \lambda_i S^{i/2}), \\ \mathrm{m}_{k/2} & = & \int_0^1 s^{k/2} \exp(-\lambda_0 - \sum_{i=1}^{N} \lambda_i s^{i/2}) ds. \end{array} \right. \tag{33}$$

The problem then consists in finding a vector $\boldsymbol{\lambda} = (\lambda_0, .., \lambda_N)$ in $\mathbb{R}^N$ which satisfies the moment equations in the system (33). This problem is equivalent to find an optimum of the potential function $G(\lambda_0, .., \lambda_N)$:

$$G(\lambda_0, \ldots, \lambda_N) = \int_0^1 \exp(-\lambda_0 - \sum_{i=1}^{N} \lambda_i S^{i/2}) dS + \sum_{k=0}^{N-1} \lambda_k \mathrm{m}_{k/2}. \tag{34}$$

The Hessian matrix H defined by $H_{i,j} = \frac{\partial^2 G}{\partial \lambda_i \partial \lambda_j}$ is a positive definite matrix, which ensures uniqueness of an eventual existing solution. ∎

LEMMA 3. *The function G, defined in (34), is a continuous function in $\mathbb{R}^N$, and goes to infinity when $||\boldsymbol{\lambda}|| \to +\infty$.*

Proof. Let us suppose that the last assertion is wrong, so there exists a sequence $(\boldsymbol{\lambda}^{(n)})_{n=0,1,..}$ such that $||\boldsymbol{\lambda}^{(n)}|| \to +\infty$ when $n \to +\infty$ and $\sup_n \left\{ G(\boldsymbol{\lambda}^{(n)}) \right\} < +\infty$.
Hence, there exists $A \in \mathbb{R}$ such that:

$$G(\boldsymbol{\lambda}^{(n)}) = \int_0^1 \exp(-\sum_{i=0}^{N} \lambda_i^{(n)} S^{i/2}) dS + \sum_{k=0}^{N} \lambda_k^{(n)} \mathrm{m}_{k/2} < A. \tag{35}$$

We write for each $n \in \mathbb{N}$, $\boldsymbol{\lambda}^{(n)} = \lambda^n(\alpha_0^{(n)}, \alpha_0^{(n)}, \ldots, \alpha_N^{(n)})$, such that $\sum_{i=0}^{N} (\alpha_i^{(n)})^2 = 1$ and $\lambda^{(n)} \to +\infty$.
Since the sequence $(\boldsymbol{\alpha}^{(n)})_{n=0,1..}$ is a bounded sequence, we can subtract a convergent subsequence $(\boldsymbol{\alpha}^{\phi(n)})_n$, where $\phi : \mathbb{N} \to \mathbb{N}$ is an increasing function and:

$$\lim_{n \to +\infty} \alpha_i^{\phi(n)} = \alpha_i. \tag{36}$$

To simplify the notation, we can directly consider that $\alpha_i^{(n)} \to \alpha_i$ when $n \to +\infty$.
We note by $Q^{(n)}(x) = \sum_{i=0}^{N} (\alpha_i^{(n)} x^{i/2})$ and $Q(x) = \sum_{i=0}^{N} \alpha_i x^{i/2}$.

Since the vector $\mathbf{m}_N = (\mathrm{m}_0, \mathrm{m}_{1/2}, .., \mathrm{m}_{(N)/2})$ is a moment vector, there exists a non-negative distribution function f such that $m_{k/2} = \int_0^1 s^{k/2} f(s) ds$ for $k = 0, \ldots N$, and

$$G(\boldsymbol{\lambda}^{(n)}) = \int_0^1 \exp(-\lambda^{(n)} Q^{(n)}(s)) ds + \int_0^1 \lambda^{(n)} Q^{(n)}(s) f(s) ds \leq A. \tag{37}$$

Since the first integral is positive

$$\int_0^1 Q^{(n)}(s)f(s)ds \leq \frac{A}{\lambda^{(n)}}. \tag{38}$$

When n tends to infinity, we get:

$$\int_0^1 Q(s)f(s)ds \leq 0. \tag{39}$$

We have $Q \neq 0$, $f \geq 0$ and $f \neq 0$, and since Q is a continuous function, it follows from the inequality (39) that there exists $[a, b] \subset [0, 1]$ in which $Q(s) \leq -B$ and $B > 0$. Since $Q^{(n)}$ converges uniformly to Q in $[0, 1]$, then, for all $s \in [a, b]$ and for the large enough values of n:

$$Q^{(n)}(s) < -B/2. \tag{40}$$

Using these results in the inequality (37), as well as $\alpha_k^n \mathrm{m}_{k/2} \geq -\mathrm{m}_0$, we get:

$$\begin{aligned} A &\geq \int_a^b (exp(-\lambda^{(n)}Q^{(n)}(s)))ds + \sum_{i=0}^N \lambda_i^{(n)} \mathrm{m}_{i/2}, \\ &\geq (b-a)exp(\lambda^{(n)}(\tfrac{B}{2})) - \lambda^{(n)} N \mathrm{m}_0, \end{aligned} \tag{41}$$

In the limit when n goes to infinity, we get the contradiction $+\infty < A$, thus concluding the proof. ∎

THEOREM 4. *If the vector* $\mathbf{m}_N = (\mathrm{m}_0, \mathrm{m}_{1/2}, .., \mathrm{m}_{(N)/2})$ *belongs to the interior of the Nth fractional moment space, then the constrained optimization* (29) *problem admits a unique solution, which is in the following form:*

$$n^{ME}(S) = \exp(-\lambda_0 - \sum_{i=1}^N \lambda_i S^{i/2}). \tag{42}$$

Proof. The proof is straightforward by using the two last lemmas. ∎

3.4. Algorithm of the NDF reconstruction through the Entropy Maximisation. The reconstruction of the NDF through the maximization of Shannon entropy goes back to finding the Lagrange's multipliers $\lambda_0 \dots \lambda_N$ such that:

$$\mathrm{m}_{k/2} = \int_0^1 S^{k/2} \exp(-(\lambda_0 + \sum_{i=1}^N \lambda_i S^{i/2})), \tag{43}$$

where $k = 0 \dots N$. Solving this nonlinear system is equivalent to optimizing the convex function $G(\boldsymbol{\lambda})$. We solve the problem by using the Newton iteration as proposed in [48]:

The integral computations are done by using Gauss-Legendre quadrature. In [48], it is shown that 24-point quadrature is very efficient to calculate accurately the different integral expressions involved in the algorithm.

4. Numerical resolution of the moment governing equations. The phenomena involved in the model can be classified in two main classes: the transport of the droplets in the physical space and the source terms, which induce the particle evolution in the phase space (velocity and size) through evaporation and drag. We use operator splitting techniques [17, 12] to separate the resolution of the different phenomena, we can then solve each operator separately.

Algorithm 1 EM algorithm

Choose initial guess of the vector $\boldsymbol{\lambda}$.
$\delta_{k/2} \leftarrow \mathrm{m}_{k/2} - \int_0^1 S^{k/2} \exp(-\sum_{i=0}^{N} \lambda_i S^{i/2})$
while $||\boldsymbol{\delta}|| > \epsilon \mathrm{m}_0$ **do**
  for $i, j < N$ **do**
    $H_{i,j} \leftarrow \int_0^1 S^{(i+j)/2} \exp(-\sum_{i=0}^{N} \lambda_i S^{i/2})$
  end for
  $\boldsymbol{\lambda} \leftarrow \boldsymbol{\lambda} - \boldsymbol{H}^{-1} \cdot \boldsymbol{\delta}$
  for $k < N$ **do**
    $\delta_{k/2} \leftarrow \mathrm{m}_{k/2} - \int_0^1 S^{k/2} \exp(-\sum_{i=0}^{N} \lambda_i S^{i/2})$
  end for
end while

4.1. Resolution of evaporation. Let us consider a pure evaporation without transport nor drag. The kinetic equation in this case reads:

$$\partial_t n - \partial_S(Kn) = 0. \tag{44}$$

The integration of this equation multiplied by the vector $(1, S^{1/2}, S, S^{3/2})^t$ yields to the system of equation of the moment in the section $[0, 1]$

$$\begin{cases} d_t \mathrm{m}_0 &= -n^{ME}|_{S=0}, \\ d_t \mathrm{m}_{1/2} &= -\dfrac{\mathrm{K}}{2} \mathrm{m}_{-1/2}, \\ d_t \mathrm{m}_1 &= -\mathrm{K} \mathrm{m}_0, \\ d_t \mathrm{m}_{3/2} &= -\dfrac{3\mathrm{K}}{2} \mathrm{m}_{1/2}, \end{cases} \tag{45}$$

where the $n^{ME}|_{S=0}(\mathrm{m}_0, \mathrm{m}_{1/2}, \mathrm{m}_1, \mathrm{m}_{3/2})$ is obtained by ME algorithm.
Solving this system using classical integrator such as Euler or Runge-Kutta methods leads to serious stability problems. In fact, classical ODE integrators do not ensure the preservation of the moments in the moment space [47]. This property is essential for robustness and accuracy to reconstruct a positive NDF.

4.1.1. Exact kinetic solution through the method of characteristics. The exact solution of the NDF evolution using a d^2 evaporation law, can be obtained easily by solving analytically the kinetic equation (44) using the method of characteristics:

$$n(t, S) = n(0, S + \mathrm{K}t). \tag{46}$$

For more general evaporation law, when the evaporation rate $\mathrm{R}_S(S)$ is a smooth function of the size, the kinetic equation is written as follows:

$$\partial_t n + \partial_S(\mathrm{R}_S(S) n) = 0. \tag{47}$$

By multiplying the equation by $\mathrm{R}_S(S)$, we obtain:

$$\partial_t \Gamma(t, S) + \mathrm{R}_S(S) \partial_S(\Gamma(t, S)) = 0, \tag{48}$$

where $\Gamma(t,S) = \mathrm{R}_S(S)n(t,S)$. For a given initial time t_0 and size s_0, we define the one variable function $g(t) = \Gamma(t, \widetilde{S}(t;t_0,s_0))$, such that $\widetilde{S}(t;t_0,s_0)$ is the characteristic curve verifying:

$$\left\{ \begin{array}{rcl} \dfrac{d\widetilde{S}(t;t_0,s_0)}{dt} & = & \mathrm{R}_S(\widetilde{S}(t;t_0,s_0)), \\ \widetilde{S}(t_0;t_0,s_0) & = & s_0. \end{array} \right. \tag{49}$$

The derivative of $g(t)$ vanishes, thus, we obtain the following expression:

$$\Gamma(t, \widetilde{S}(t;t_0,s_0)) = \Gamma(t_0,s_0). \tag{50}$$

Finally, we obtain the exact solution of the size distribution as follows:

$$n(t,S) = \frac{\mathrm{R}_S(\widetilde{S}(t_0;t,S))}{\mathrm{R}_S(S)} n(t_0, \widetilde{S}(t_0;t,S)) \tag{51}$$

4.1.2. Fully kinetic scheme. At each time step t_n, the reconstructed NDF $n^{ME}(t=t_n,S)$ is determined using ME algorithm, then the exact kinetic solution of the NDF can be expressed analytically as a function of this initial NDF thanks to (46). Finally, the updated moments are computed as follows:

$$\begin{array}{rcl} \mathrm{m}_{k/2}(t_n+\Delta t) & = & \int_0^1 S^{k/2} n(t_n+\Delta t, S) dS \\ & = & \int_{K\Delta t}^1 (S-K\Delta t)^{k/2} n^{ME}(t_n, S+K\Delta t) dS, \end{array} \tag{52}$$

The calculation of this integral can be achieved by using Gauss-Legendre quadrature as previously. The method is simple and accurate. However, its extension to complex evaporation law, where the evaporation rate depends on several parameters, could lead to heavy calculations. To clarify this point, we consider a smooth evaporation law, where $\mathrm{R}_S(S)$ depends on the droplet size. Considering the exact kinetic solution (51), we can obtain the following expression:

$$\mathrm{m}_{k/2}(t_{n+1}) = \int_{\widetilde{S}(t_n;t_{n+1},0)}^1 \widetilde{S}(t_{n+1};t_n,s)^{k/2} n(t_n,s) ds. \tag{53}$$

To compute this integral, we need to determine the size $\widetilde{S}(t_{n+1},t_n,S_j)$, for each abscissa S_j of the 24-quadrature points, by solving the ODE system (49).

4.1.3. Inefficiency of the original EMSM algorithm for evaporation. Massot et al [47] proposed a realizable algorithm to solve correctly the evaporation moment system in the case of integer moment. The idea of this algorithm is also based on the known solution of the kinetic equation (44). In order to generalize the d^2 evaporation law for more complex laws, the calculation of the moments was done in three steps instead of computing directly the integral formulas (52) in the case of d^2 law or (53) in general case using a large number of Gauss-Legendre quadrature. This algorithm reads in the case of fractional moments as follows:

- From the moment vector $\mathbf{m}(t_n) = (\mathrm{m}_0, \mathrm{m}_{1/2}, \mathrm{m}_1, \mathrm{m}_{3/2})^t$, we reconstruct NDF by using the ME algorithm. Then, we compute the disappearance flux, which represents the droplets which will be totally evaporated at the next step:

$$\mathbf{\Phi}_- = \int_0^{K\Delta t} n_{ME}(t_n,S) \begin{pmatrix} 1 \\ S^{1/2} \\ S \\ S^{3/2} \end{pmatrix} dS. \tag{54}$$

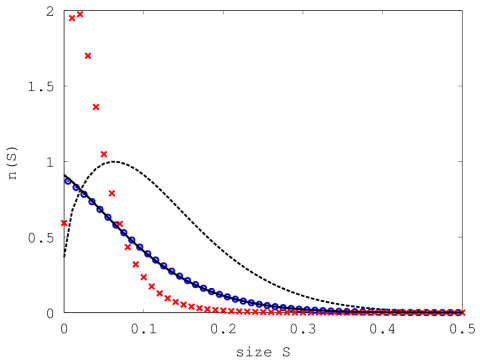

Fig. 1: Initial size distribution (dashed line) and the reconstructed size distribution at $t = 0.2$ using: exact kinetic solution (solid line), EMSM algorithm (cross), fully kinetic scheme (circle)

- The abscissas $S_j \geq \mathrm{K}\Delta t$ and the weights $w_j \geq 0$ corresponding to the lower principal representation (111) of the moments[1] $\mathbf{m}^{[\mathrm{K}\Delta t,1]}(t_n) = \mathbf{m}(t_n) - \mathbf{\Phi}_-(t_n)$ are computed by using the PD algorithm [29].

$$m_{k/2}^{[\mathrm{K}\Delta t,1]} = \sum_{j=1}^{2} w_j S_j^{k/2}, \tag{55}$$

  where $\mathbf{m}^{[\mathrm{K}\Delta t,1]}(t_n)$ is the moment vector in the support $[K\Delta t, 1]$.
- We calculate the moments at the next step:

$$\mathrm{m}_{k/2}(t_n + \Delta t) = \sum_{j=1}^{2} w_j (S_j - \mathrm{K}\Delta t)^{k/2}. \tag{56}$$

In Figure 1, we compare the evolution of the reconstructed NDF from the moments computed with the fully kinetic algorithm, the reconstructed NDF from the moments computed with the above algorithm and the exact kinetic solution. The results show the inefficiency of this last algorithm to predict the right kinetic evolution of the NDF, when we use fractional moments. In the next section, we give a mathematical development of the exact kinetic solution of the fractional moment (52) in order to understand the limitation of this algorithm, then we propose a new original solution to adapt the algorithm.

4.1.4. Adapted evaporation scheme for fractional moments. In this section, we rewrite the updated moment as a function of an initial infinite set of moments on the support $[\mathrm{K}\Delta t, 1]$. This result will allow us to identify the missing point in the last algorithm. Then, a correction of the algorithm is proposed at the end of the section as well as its extension to more general evaporation laws.

[1] We can also use hybrid approach with multi-size sections, in this case we need to take into account the evaporation fluxes coming from the right section: $\mathbf{m}(t_n) - \mathbf{\Phi}_-^{(i)}(t_n) + \mathbf{\Phi}_-^{(i+1)}(t_n)$, where i indexes the section.

LEMMA 5. *For all positive integer k and for all $x \in [-1,1]$ the function $f : x \to (1-x)^{k/2}$ admits a power series which converges normally to the function f.*

Proof. The case of k is an even integer is trivial. Let us consider the case where $k = 2m+1$ is an odd number. The function f admits a power series and the convergence radius of the series is 1, and we for all $|x| < 1$:

$$(1-x)^{k/2} = \sum_{n=0}^{+\infty} a_n^{k/2} x^n, \tag{57}$$

we can show that the coefficients $a_n^{k/2}$ can be written as follows:

$$a_n^{k/2} = (-1)^{m+1} \frac{(2(n-m-1))!(2m+1)!}{(n-m-1)!m!2^{2n-1}n!}. \tag{58}$$

Now, by using the Stirling's approximation:

$$n! \sim \sqrt{2\pi n}\left(\frac{n}{e}\right)^n. \tag{59}$$

We can prove the following equivalence relation when n tends to infinity.

$$|a_n^{k/2}| \sim \frac{(2m+1)!}{4^m\sqrt{\pi}m!}\frac{1}{n^{3/2+m}}. \tag{60}$$

Therefore the series $\sum |a_n^{k/2}|$ is convergent for any positive integer $k \geq 0$. ∎

We deduce that $\sum_{n=0}^{\infty} a_n^{k/2}(\mathrm{K}\Delta t)^n s^{k/2-n}$ converges normally to $(s-\mathrm{K}\Delta t)^{k/2}$ for $s \geq \mathrm{K}\Delta t$. Thus, We can invert the sum and the integral in the moment expression:

$$\begin{aligned} \mathrm{m}_{k/2}(t+\Delta t) &= \sum_{n=0}^{\infty} a_n^{k/2}(\mathrm{K}\Delta t)^n \int_{\mathrm{K}\Delta t}^1 s^{k/2-n} n(t,s)ds \\ &= \sum_{n=0}^{\infty} a_n^{k/2}(\mathrm{K}\Delta t)^n \mathrm{m}_{k/2-n}^{[\mathrm{K}\Delta t,1]}(t) \end{aligned} \tag{61}$$

Equation (61) shows that the fractional moment at $t+\Delta t$ depends on an infinite set of the moments of support $[\mathrm{K}\Delta t, 1]$ ($m_a^{[\mathrm{K}\Delta t,1]}$ where $a = k/2, k/2-1, \ldots -\infty$). In the case of the EMSM model, where only integer moments are used in the model, the same expansion of the exact kinetic solution of the integer moment involves only the four transported moments. For this reason, the evolution of the moment can be evaluated exactly by translating the abscissas (56) of the lower principal representation (55), which is not the case for the present model. Therefore, we need an adapted quadrature instead of the one used in (55), such that the moment evolution in the equation (56) approximates accurately the exact kinetic evolution (61).

DEFINITION 6. *We consider a density function μ of the support $[a,b]$. The abscissas $(x_j)_{j=1\ldots n}$ in $[a,b]$ and the weights $(w_j)_{j=1\ldots n} > 0$ are called Gauss quadrature rule of order n corresponding to μ if and only if for all polynomial function $p \in \mathbb{P}_{2n-1}$ of degree $\leq 2n-1$, we have:*

$$\int_a^b p(x)\mu(x)dx = \sum_{j=1}^{n} w_j p(x_j) \tag{62}$$

The existence of such quadrature for each positive measure is proved in [28]. The Gauss quadrature of order n is also the lower principal representation (see Appendix B) associated to the $2n$ first integer moment of measure μ.

Our objective is to find an adequate Gauss quadrature with the lowest possible quadrature number n_q, such that the following approximation

$$\mathrm{m}_{k/2}(t+\Delta t) \approx \sum_{j=1}^{n_q} w_j (S_j - K\Delta t)^{k/2} \tag{63}$$

is accurate. More precisely, we would like to find an adequate Gauss quarature such that the difference

$$\begin{aligned} \epsilon_{k/2}(\Delta t) &= \mathrm{m}_{k/2}(t+\Delta t) - \sum_{j=1}^{n_q} w_j (S_j - \mathrm{K}\Delta t)^{k/2} \\ &= \sum_{n=0}^{\infty} a_n^{k/2} (\mathrm{K}\Delta t)^n \left(m_{k/2-n}^{[\mathrm{K}\Delta t,1]}(t) - \sum_{j=1}^{n_q} w_j S_j^{k/2-n} \right). \end{aligned} \tag{64}$$

is at least $o(\Delta t)$ to ensure the convergence of the numerical scheme. Unfortunately, it is a difficult task to prove this point and this problem goes back to seeking for an accurate estimation of the Gauss quadrature errors [28]. However, the task of providing a rigorous proof of the convergence is beyond of the objective of the present paper. In the following, we focus on practical issues and we will present a general strategy to decrease the error $\epsilon_{k/2}(\Delta t)$ by cancelling a finite set of first terms in the infinite sum (64). We mention that for even k the error $\epsilon_{k/2} = 0$.

Let us consider the measure $\widetilde{\mu}(r) = \frac{2rn(r^2)}{r^{2n_q^-}}$, where n_q^- is a positive integer variable, defined in the support $[\sqrt{\mathrm{K}\Delta t}, 1]$ for the variable[2] $r = \sqrt{S}$. Then, the Gauss quadrature of order $n_q = n_q^- + 2$ of the measure $\widetilde{\mu}(r)$, represented by the abscissas r_j and weights w'_j, satisfies:

$$\begin{aligned} \sum_{j=1}^{n_q} w'_j r_j^k &= \int_{\sqrt{\mathrm{K}\Delta t}}^1 r^k \widetilde{\mu}(r) dr, \\ &= \int_{\mathrm{K}\Delta t}^1 s^{k/2-n_q^-} n(s,t) ds, \\ &= \mathrm{m}_{k/2-n_q^-}^{[\mathrm{K}\Delta t,1]}(t), \end{aligned} \tag{65}$$

for $k = 0 \dots 2n_q - 1$ ($k = 0 \dots 2n_q^- + 3$). The computation of the weights w'_j and the abscissas r_j can be determined by the PD algorithm [29]. The coefficients w_j and S_j are defined as follows:

$$\left\{ \begin{array}{rcl} w_j &=& w'_j r^{n_q^-} \\ S_j &=& \sqrt{r_j} \end{array} \right. \tag{66}$$

and they verify for all $k = -2n_q^-, \dots, 3$:

$$\mathrm{m}_{k/2}^{[\mathrm{K}\Delta t]} = \sum_{j=1}^{n_q} w_j S_j^{k/2}. \tag{67}$$

[2]This substitution makes the link between the fractional moment and its corresponding integer moment – see Appendix B.

By using this quadrature in the equation (64), we cancel the $k+n_q^-$ first terms in the series ($k \in \{0,1,2,3\}$ positive moment orders and n_q^- negative moment orders):

$$\epsilon_{k/2}(\Delta t) = \sum_{n=n_q}^{+\infty} a_n^{k/2} (K\Delta t)^n \left(\mathrm{m}_{-n-k/2}^{[\Delta t,1]}(t) - \sum_{j=1}^{n_q} w_j S_j^{-n-k/2} \right) \Delta t^{k/2}. \tag{68}$$

From these results we conclude that, the exact moment evolution depends on other moments than the ones involved in the moment system (26). More precisely, the computation of the kinetic evolution depends on an infinite set of moment of negative order. Thus, the missing point in the last algorithm, developed mainly for integer moment, consists in limiting the lower principal representation (55) to the moment on the support $[\mathrm{K}\Delta t, 1]$ used in the model (the four fractional moments), which also corresponds to take $n_q^- = 0$. In order to correct this default, we need at least to consider some moment of negative order in the low principal representation $n_q^- > 0$. However, we do not know theoretically the sufficient number of quadrature nodes needed to approximate the solution. In fact, this problem goes back again to the convergence issue of this method. Since, we do not provide of a complete proof, we rely on the numerical results to identify the necessary number of quadrature nodes. The results show that for $n_q^- = 1$, where two supplementary moment of negative order ($m_{-1/2}^{[\Delta t,1]}$ and $m_{-1}^{[\Delta t,1]}$) are represented by the quadrature, the solution approximates accurately to the exact kinetic solution. Some of these results are presented in Section 6. This is an important result, since we need only a total of three quadratures $n_q = 3$ to capture the kinetic evolution. Besides, we can use more quadrature points to increase the precision by choosing $n_q^- \geq 2$. Let us underline that the proper approximation and closure of the negative moments is here a key issue.

New adapted algorithm. According to the last results, we propose an adapted 4-steps algorithm. This algorithm is named **NEMO** (Negative Moments) algorithm and described below:

A. We reconstruct $n^{ME}(S)$ corresponding to the moment vector $\mathbf{m}(t_n)$ by ME algorithm, then we calculate the disappearance flux

$$\mathbf{\Phi}_-(t_n) = \int_0^{\mathrm{K}\Delta t} n^{ME}(t=t_n, s) \begin{pmatrix} 1 \\ s^{1/2} \\ s \\ s^{3/2} \end{pmatrix} ds. \tag{69}$$

B. We calculate the negative order moments at the interval $[K\Delta t, 1]$

$$\mathrm{m}_{-a/2}^{[K\Delta t,1]} = \int_{\mathrm{K}\Delta t}^1 s^{-a/2} n^{ME}(s) ds, \tag{70}$$

for $a = 1, \ldots, 2n_q^-$, where $2n_q^- \geq 2$ is the number of additional moments of negative order used in this algorithm and chosen by the user. The other moments of positive order are computed using the disappearance flux:

$$\mathrm{m}_{k/2}^{[\mathrm{K}\Delta t,1]} = \mathrm{m}_{k/2}(0) - \Phi_{-,k/2}(t_n), \quad k = 0\ldots,3 \tag{71}$$

C. The abscissas $S_j \in [\mathrm{K}\Delta t, 1]$ and the weights w_j corresponding to the lower principal representation of the moments $m_{l/2}^{[\mathrm{K}\Delta t,1]}$ for $l = -2n_q^-, \ldots, 3$ are

computed using PD Algorithm [29] and the relations (66), such that:

$$m_{l/2}^{[\mathrm{K}\Delta t,1]} = \sum_{j=1}^{n_q} w_j S_j^{l/2}, \tag{72}$$

where $n_q = n_q^- + 2$.

D. Finally, we calculate the updated moments as follows:

$$\mathrm{m}_{k/2}(t_n + \Delta t) = \sum_{j=1}^{n_q} w_j (S_j - \mathrm{K}\Delta t)^{k/2}. \tag{73}$$

The singularities of the negative moment integral, when Δt is very small, limits the use of high values of n_q^-. But in practice $\Delta t > 1.e-4$ and we will show that the choice of $n_q^- = 1$ or $n_q^- = 2$ are sufficient to obtain an accurate solution. In these cases, the integral computation of the negative order moment can be achieved correctly with 24-point quadrature of Gauss-Legendre quadrature as for the other moments.

For more complex evaporation laws, the algorithm can be generalized by computing the Lagrangian evolution of the abscissas. In other words, the equation (73) becomes:

$$\mathrm{m}_{k/2}(t_n + \Delta t) = \sum_{j=1}^{n_q} w_j \widetilde{S}(t_n + \Delta t; t_n, S_j)^{k/2}. \tag{74}$$

4.2. Evaporation coupled with drag. In this paragraph, we present a coupled solver for the spray evolution under evaporation and drag force. The corresponding system of equations reads:

$$\left\{ \begin{array}{rcl} d_t \mathrm{m}_0 & = & -n(S=0), \\ d_t \mathrm{m}_{1/2} & = & -\dfrac{\mathrm{K}}{2}\mathrm{m}_{-1/2}, \\ d_t \mathrm{m}_1 & = & -\mathrm{K}\mathrm{m}_0, \\ d_t \mathrm{m}_{3/2} & = & -\dfrac{3\mathrm{K}}{2}\mathrm{m}_{1/2}, \\ d_t \left(\mathrm{m}_1 \boldsymbol{U}\right) & = & -\mathrm{K}\mathrm{m}_0 \boldsymbol{U} + \mathrm{m}_0 \dfrac{\boldsymbol{U}_g - \boldsymbol{U}}{\theta}. \end{array} \right. \tag{75}$$

Since the first four equations do not depend on the last equation, the moments are computed using the algorithm presented in the last section. We use the method developed in [64] to solve the evolution of the velocity by the drag force coupled with evaporation.

The momentum evolution is conducted in two steps: first, we remove the part of the droplets, which will completely evaporated during the time interval $[t_n, t_{n+1}]$, by evaluating the disappearance fluxes of the moments and momentum:

$$\mathcal{U}^{[\mathrm{K}\Delta t,1]} = \mathcal{U} - \begin{pmatrix} \boldsymbol{\Phi}_- \\ \Phi_{-,1}\boldsymbol{U} \end{pmatrix}, \tag{76}$$

where $\mathcal{U} = (\mathrm{m}_0, \ldots, \mathrm{m}_{3/2}, \mathrm{m}_1 \boldsymbol{U}^t)^t$ and $\boldsymbol{\Phi}_-$ is the disappearance flux vector of the moments (69). Then, we use the lower principal representation to approximate the

size distribution of the moment of the support $[\mathrm{K}\Delta t, 1]$ (72). The computation of the moments is achieved with (73). And to evaluate the momentum evolution in this last step, we consider a correlated size-velocity, such that, at a given time $t \in [t_n, t_{n+1}]$, we attribute the velocity $\boldsymbol{c}_i(t)$ to each abscissa $S_i(t)$ of the lower principal representation. Then, we compute the momentum as flows:

$$(\mathrm{m}_1\boldsymbol{U})^{[\mathrm{K}\Delta t,1]}(t_{n+1}) = \sum_{i=1}^{n_s} w_i S_i(t_{n+1})\boldsymbol{c}_i(t_{n+1}), \tag{77}$$

where $t \in [t_n, t_{n+1}]$, and the abscissas $S_i(t_{n+1})$ and the velocities $\boldsymbol{c}_i(t_{n+1})$ are determined by solving the following ODE systems:

$$\left\{\begin{array}{rcl} \dfrac{d\boldsymbol{c}_i}{dt} & = & -\dfrac{\boldsymbol{U}_g - \boldsymbol{c}_i}{\theta S_i}, \\ \dfrac{dS_i}{dt} & = & -\mathrm{K}, \\ S_i(t=t_n) & = & S_i(t_n), \\ \boldsymbol{c}_i(t=t_n) & = & \boldsymbol{U}(t_n), \end{array}\right. \tag{78}$$

Then, the momentum and the final cell velocity are computed as follows:

$$\begin{array}{rcl} (\mathrm{m}_1\boldsymbol{U})^{n+1} & = & \sum\limits_{i=1}^{n_s} w_k S_i(t_{n+1})\boldsymbol{c}_i(t_{n+1}), \\ \boldsymbol{U}(t_{n+1}) & = & \dfrac{(\mathrm{m}_1\boldsymbol{U})^{n+1}}{\mathrm{m}_1^{n+1}}. \end{array} \tag{79}$$

This method can be generalized to more complex evaporation law by replacing $-\mathrm{K}$ in the equation (78) by a general evaporation rate $\mathrm{R}_S(S)$.

5. Transport scheme in physical space: adapted EMSM approach. We choose to present the scheme in a two dimensional space to lighten the notations and we note $\boldsymbol{U} = (u, v)$. For the transport resolution in physical space, we use a dimensional splitting algorithm. In this context we consider a free transport in one direction (we present the x-direction here) of the droplets without the evaporation nor the drag force.

$$\begin{array}{rcl} \partial_t \mathrm{m}_{k/2} + \partial_x(\mathrm{m}_{k/2}u) & = & 0, \\ \partial_t(\mathrm{m}_1\boldsymbol{U}) + \partial_x(\mathrm{m}_1 u\boldsymbol{U}) & = & 0, \end{array} \tag{80}$$

where $k = 0 \ldots 3$.

The mathematical structure of the pressureless gas system leads to some singularities (known as δ-shocks). These singularities occur when the monokinetic assumption is violated. This can happen when trajectory crossings take place and lead to particles accumulation in a very small volume. Following the idea of de Chaisemartin [10], Kah et al [38] developed a finite volume kinetic scheme for the EMSM model. We use the same approach to solve numerically the system (80). In the following, we present briefly the main steps to derive the kinetic scheme for the system (80):

A. We write the equivalent kinetic system to the pressureless system (80), as it was proposed in [6]:

$$\left\{\begin{array}{c} \partial_t f + \partial_x(c_x f) = 0 \text{ , and} \\ f(t, x, \boldsymbol{c}, S) = n(t, x, S)\delta(\boldsymbol{c} - \boldsymbol{U}), \end{array}\right. \tag{81}$$

B. We use the finite volume descritization of the system (80):

$$\begin{aligned} \mathbf{m}_i^{n+1} &= \mathbf{m}_i^n - \frac{\Delta t}{\Delta x}(F_{i+1/2} - F_{i-1/2}), \\ \boldsymbol{p}_i^{n+1} &= \boldsymbol{p}_i^n - \frac{\Delta t}{\Delta x}(G_{i+1/2} - G_{i-1/2}). \end{aligned} \tag{82}$$

C. We express the exact finite volume fluxes as function of the NDF $f(t, x, \boldsymbol{c}, S)$.

D. We split the fluxes in two integral parts: the first (resp the second) corresponds to the droplet of positive (resp negative) velocity in x-direction $(F^+_{i+1/2}, G^+_{i+1/2})^t$ resp$((F^-_{i+1/2}, G^-_{i+1/2})^t)$. Then, we use the exact solution of the kinetic system (81), to express the fluxes as function of the NDF at $t = t_n$.

E. Finally, the fluxes are expressed as function of the known moments and velocities at $t = t_n$:

$$\begin{pmatrix} F^{\pm}_{i+1/2} \\ G^{\pm}_{i+1/2} \end{pmatrix} = \frac{1}{\Delta t} \int_{x_{i-1/2}}^{x_{i+1/2}} \begin{pmatrix} \mathrm{m}_0(t_n, x) \\ \mathrm{m}_{1/2}(t_n, x) \\ \mathrm{m}_1(t_n, x) \\ \mathrm{m}_{3/2}(t_n, x) \\ \mathrm{m}_1 u(t_n, x) \\ \mathrm{m}_1 v(t_n, x) \end{pmatrix} \mathbb{1}_{\Sigma^{\pm}}(x) dx, \tag{83}$$

where $\Sigma^{\pm} = \left\{ x^{'}, \pm(x_{i+1/2} - \Delta t u(t_n, x^{'})) < \pm x^{'} \right\}$

In Appendix C, we present two numerical kinetic schemes of first and second order, which follow this strategy.

6. Numerical results. This section is dedicated to some representative test-cases and analysis of numerical results, to verify the robustness and the accuracy of the proposed numerical schemes. In the first part, we test the new evaporation algorithm in the case of d^2 law with K = 1 for two different initial conditions. A complementary evaporation test in the case of non constant evaporation rate is given in Appendix D. The second part focuses on two cases of transport in $1D$. First, we test the accuracy of the kinetic schemes dedicated to the transport. Second, a critical case of a δ-shock is performed to evaluate the robustness of the schemes. Finally, a 2D case of an evaporating spray in the presence of a steady gas field, given by Taylor-Green vortices, is presented, in order to qualify the robustness and accuracy of the method compared to EMSM.

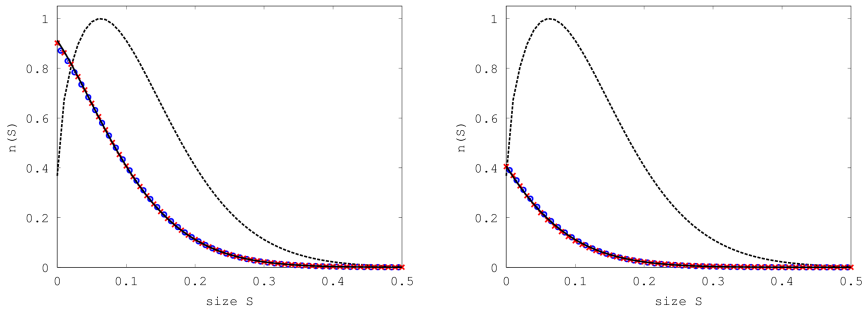

(a) t=0.1 (b) t=0.2

Fig. 2: Solutions of the reconstructed size distribution using: **NEMO** with $n_q^- = 1$ (cross), fully-kinetic (circle), exact kinetic solution (solid line), at time $t = 0.1$ and $t = 0.2$ and the initial distribution (dashed line).

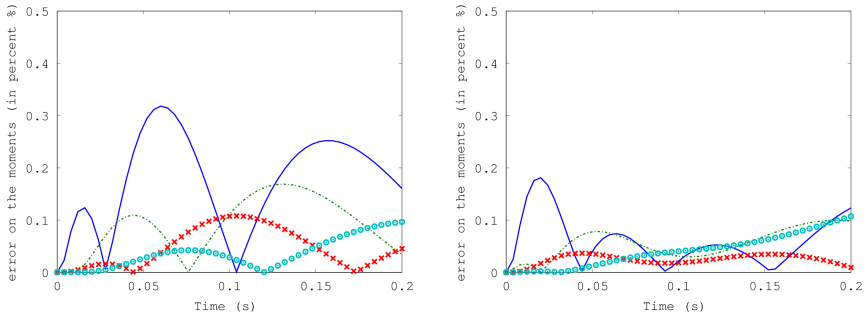

(a) Fully kinetic algorithm (b) **NEMO** algorithm with $n_q^- = 1$

Fig. 3: Evolution of the moment relative errors calculated with fully kinetic algorithm (left) and **NEMO** algorithm (right): m_0 (solid line), $m_{1/2}$ (Dash-dotted line), m_1 (cross) and $m_{3/2}$ (circle).

6.1. Evaporation in 0D simulation.

6.1.1. Evaporation with d^2 law for an initial smooth NDF. We consider an initial NDF in the form of the ME-reconstruction NDF, which is the same initial condition as the one used in Figure 1.

$$n^0(S) = exp(-20(S^{1/2} - 1/4)^2(S^{1/2} + 1)). \tag{84}$$

In this section, we compare the fully-kinetic and **NEMO** algorithms ($n_q^- = 1$), using the time step $\Delta t = 0.002$, with the exact kinetic solution. One can see from Figure 2, where we plot the reconstructed NDFs of the two algorithms and the exact kinetic distrubution at $t = 0.1$ and $t = 0.2$, that the two ME-reconstructed distributions follow accurately the exact distribution. Let us recall that for the fully-kinetic algorithm, this result is obvious, since we use a large number of quadrature to evaluate this evolution. But the important result is the one of **NEMO** algorithm, where we

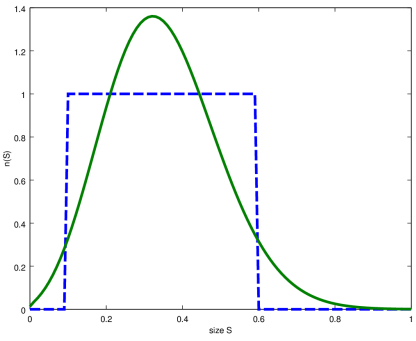

Fig. 4: The ME reconstructed NDF in the solid line and the initial discontinuous NDF in the dashed line.

have used only three quadrature nodes to capture accurately the kinetic evolution. To make a more quantitative comparison, Figure 3 shows the evolution of the relative error of the four fractional moments. We can see that in the two algorithm the moments errors relatively to the initial values do not exceed 0.3%.

6.1.2. d^2 law evaporation for a discontinuous initial NDF. In this second case, we test the new algorithm **NEMO** in the case of a discontinuous initial NDF:

$$n^0(S) = \begin{cases} 1, & \text{if } S \in [0.1, 0.6] \\ 0, & \text{otherwise} \end{cases} \tag{85}$$

The initial NDF defined in (85) and the initial ME reconstructed NDF are plotted in Figure 4.

In Figure 5, we present the reconstructed NDF computed using **NEMO** algorithm with $n_q^- = 1$ at two different times. In the same figures, we compare the obtained results with the reconstructed NDF obtained with the fully kinetic solution and the exact kinetic solution [3]. As in the previous case, **NEMO** algorithm shows an accurate prediction of the exact kinetic solution. Furthermore, Figure 6 shows that the relative error of the moments are less than 1.%, in the case of **NEMO** algorithm with $n_q^- = 1$ and $\Delta t = 6.e-3$, which is an accurate result. But, we can see that the fully-kinetic algorithm is more accurate and the moment relative errors do not exceed 0.3%. We can improve the accuracy of **NEMO** algorithm by using a small time step $\Delta t = 6.e-4$ or by using $n_q^- = 2$ and keeping the same time step as the previous case. These two results are presented in Figure 7.

6.2. Transport in 1D simulation. In this part, we investigate the accuracy and robustness of the transport schemes, the first order and the second order presented in Appendix C. The evaporation and the drag force are not considered in this study. First, we investigate the order of accuracy of the transport schemes. Then, we test the two numerical schemes in a critical case, where we generate a δ-shock singularity.

[3] The exact kinetic solution is computed for the initial ME reconstructed size distribution.

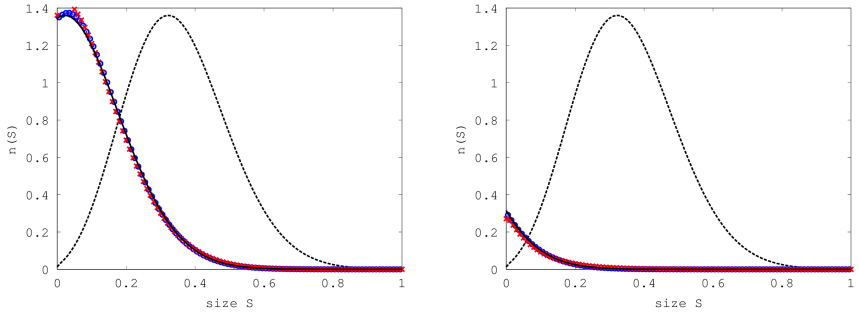

(a) t=0.3 (b) t=0.6

Fig. 5: Solutions of the reconstructed size distribution using: **NEMO** with $n_q^- = 1$ (cross), fully-kinetic (circle), exact kinetic solution (solid line), at time $t = 0.1$ and $t = 0.2$ and the initial distribution (dashed line).

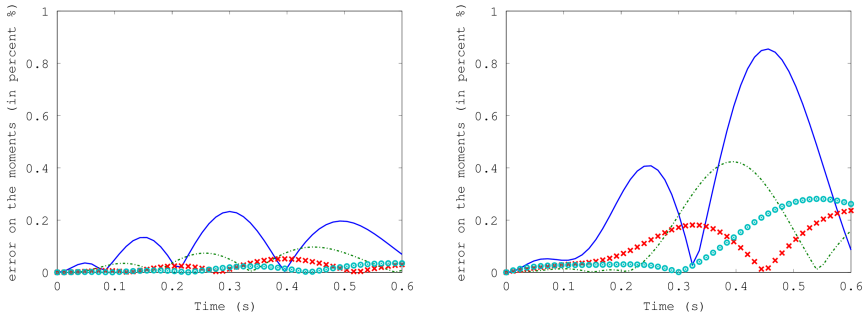

(a) Fully kinetic algorithm $dt = 6.e^-3$ (b) **NEMO** : $n_q^- = 1$ and $dt = 6.e - 3$

Fig. 6: Evolution of the moment errors relatively to their initial value calculated with fully kinetic algorithm (left) and **NEMO** algorithm (right): m_0 (solid line), $m_{1/2}$ (dash-dotted line), m_1 (cross) and $m_{3/2}$ (circle).

6.2.1. Accuracy order study. We consider an initial size distribution with a form depending on the coordinate space x. In fact, we need a non trivial initial size-space distribution, such that the slopes used in the second order scheme do not vanish all the time. The chosen initial size distribution has the following profile:

$$n(t,S,x) = 10\exp\left(-\frac{(x-x_c)^2}{\sigma_x^2}\right)\exp\left(-\frac{(\sqrt{S}-(1-x)/2)^2}{\sigma_R})\right), \tag{86}$$

where $x_c = 0.25$, $\sigma_x = 0.1$ and $\sigma_R = 0.3$. The initial velocity field is initiated as follows:

$$\left\{\begin{array}{lcll} u(t=0,x) & = & 0.5-x & x<0.5, \\ u(t=0,x) & = & 0. & x\geq 0.5 \end{array}\right. \tag{87}$$

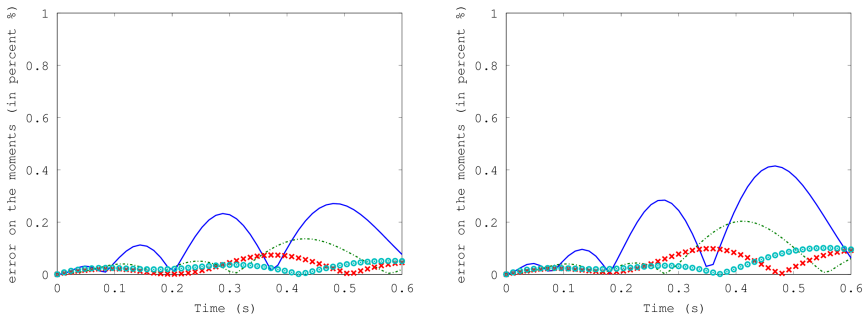

(a) **NEMO** : $n_q^- = 2$ and $\Delta t = 6e-3$ (b) **NEMO** : $n_q^- = 1$ and $\Delta t = 6e-4$

Fig. 7: Evolution of the moment errors relatively to their initial value calculated with **NEMO** algorithm with $n_q^- = 2$ and $\Delta t = 6e-3$ (left) $n_q^- = 1$ and $\Delta t = 1e-4$ (right): m_0 (solid line), $\mathrm{m}_{1/2}$ (Dash-dotted line), m_1 (cross) and $\mathrm{m}_{3/2}$ (circle).

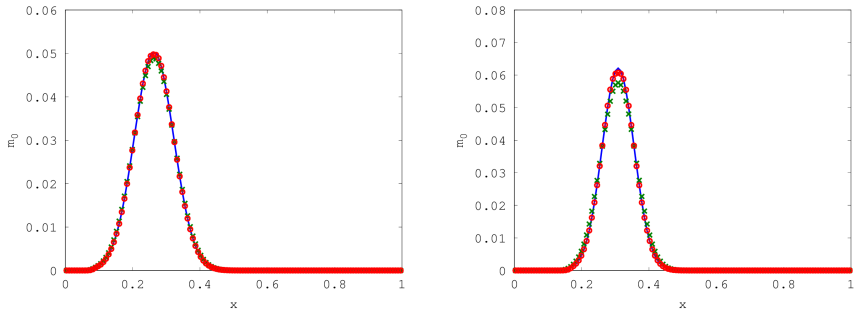

(a) $t = 0.4$ (b) $t = 0.8$

Fig. 8: Spatial profile of the moment m_0 at two different times $t = 0.4$ (left figure) and $t = 0.8$ (right figure), using 128 grid cells.

Figure 8 shows the spatial distribution of the moment m_0 obtained with the first and second order schemes at two different times ($t = 0.4$ and $t = 0.8$). Comparing the two schemes, it is clear that the results obtained with the second order scheme are more accurate than the ones obtained with the first order. In Figure 9, we show the grid convergence for the first and second order to the analytic solution at $t = 0.8$. The second order scheme converges faster than the first order scheme to the solution. In the extremum of the moment spatial profile, we can see that the convergence to solution is slow compared to the other points. In fact, the slope limitation in this point is activated to ensure a non oscillating solution, but, it introduces some numerical diffusion. To go further in this analysis, we compute the L^1-error for each numerical scheme depending on the grid size. In Figure 10, we display the order curve for the two schemes. As it can be seen from these curves, the order of the first order scheme is around 0.6 and of the second order, around 1.5.

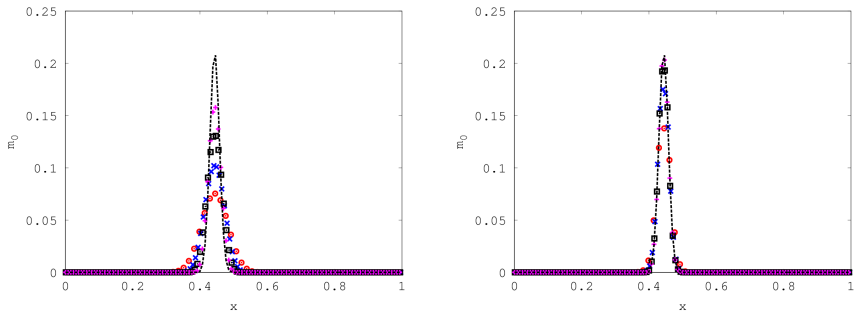

(a) the first order scheme (b) the second order scheme

Fig. 9: The gird convergence for the first order scheme (left) and the second order scheme (right). The curves correspond: (circle) 64 cells, (cross) 128 cells, (square) 256 cells, (plus) 512 cells and (dashed-line) exact solution.

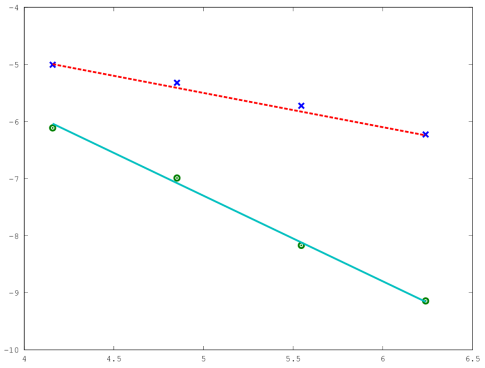

Fig. 10: Error curves with respect to grid refinement in logarithmic scale: the line $y = 1.5\log(\Delta x)+0.2$ (solid line), the line $y = 0.6\log(\Delta x)-2.5$ (dashed-line), logarithm error of m_0 using second order (cross symbol) and logarithm error of m_0 using first order (circle symbol).

6.2.2. Robustness and capacity of capturing δ-shocks. The monokinetic-assumption is not a valid hypothesis when droplets cross. In such an event, the monokinetic-model generates a δ-shock. Despite the non-physical solution, the two kinetic schemes should be able to run in all critical situations and even resolve the created singularities. In this section, we test the robustness of the numerical schemes in a case of a strong crossing. Initially, we consider two spatial Gaussian distributions centered at two positions and traveling at opposite velocity as shown in Figure 11.

Figure 12 shows the spatial profile of the moment m_0 at two different times. We can see the shock generation when the two packets cross. At the end, the droplets accumulate at the center and the corresponding spacial distribution is in the form of a delta Dirac measure.

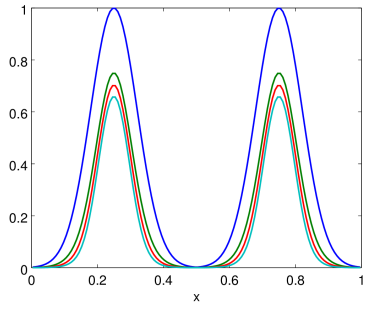

(a) Initial moments: the cures represent the moment with decreasing order in terms of value.

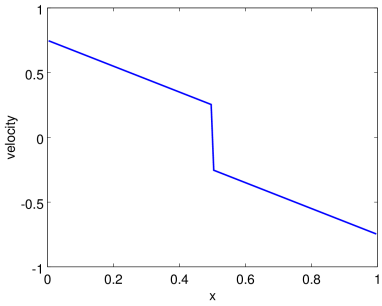

(b) Initial velocity

Fig. 11: Initial condition for the crossing case.

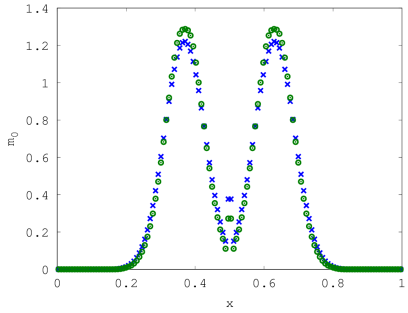

(a) $t = 0.6$

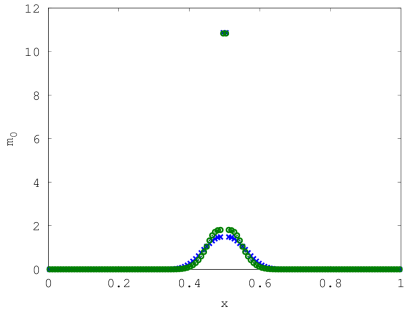

(b) $t = 1.2$

Fig. 12: The spatial profile of the moment m_0 in the crossing case. The results are given for 128 cells for both first order scheme (cross) and second order (circle) schemes.

6.3. 2D simulation: Transport, evaporation and the drag force. After the model and numerical schemes have been tested in 0D and 1D simulations, we propose in this part to compare in a classical 2D configuration the present model and numerical schemes with the EMSM model, in a case where we consider transport, evaporation and drag. The simulations are performed using the CanoP code, developed within the collaboration of Maison de la Simulation, IFPEn and EM2C Laboratory [20, 25] based on the `p4est` library [8], which has the Adaptive Mesh Refinement (AMR) capability as well as the ability to manage such meshes in massively parallel computations. Parallel performance of the code have been already evaluated in [20, 25]. In the present simulation, we use only a uniform grid, since we are not concerned with AMR in the present work. In the following, we consider an evaporating spray in the presence of Taylor-Green vortices for the gas, which is a steady solution of the inviscid incompressible Euler equations. The non-dimensional velocity

field of the gas is given as follows:

$$\begin{aligned} u_g(x,y) &= \sin(2\pi x)\cos(2\pi y), \\ v_g(x,y) &= -\cos(2\pi x)\sin(2\pi y), \end{aligned} \tag{88}$$

where $(x,y) \in [0,1]^2$ and we consider periodic boundary conditions. Initially, the spray is localized in the bottom-left vortex. The initial spatial size-distribution is given as follow:

$$n(t,\boldsymbol{x},S) = 1_{[a,b]}(S) 1_{\left\{\boldsymbol{x}', ||\boldsymbol{x}-\boldsymbol{x}_c||_2 < \sqrt{2}r\right\}}(\boldsymbol{x}) \exp(-||\boldsymbol{x}-\boldsymbol{x}_c||_2^2/r^2), \tag{89}$$

where $[a,b] = [0.25, 0.75]$, $\boldsymbol{x}_c = (0.15, 0.15)$ and $r = 0.1$. The initial Stokes number computed with the mean size $\bar{S} = \mathrm{m}_1/\mathrm{m}_0$ is equal to $\mathrm{St}(\bar{S}) = 0.05$, that is close to the critical Stokes number. The Stokes number decreases over the time because of evaporation. The spray evaporation rate is $\mathrm{K} = 0.5$. In Figures 13-14, we present the computed spatial distribution of the volume fraction at two different times: using the EMSM model (left) and the new fractional moment model (right). We have used second order scheme for the transport resolution in both cases and the EMSM evaporation algorithm to solve evaporation in the EMSM model and **NEMO** algorithm with $n_q^- = 1$ for fractional moments. For the EMSM model, the volume fraction is not resolved but it is calculated through ME reconstruction of the size distribution $(1/\sqrt{6\pi}) \int_0^1 S^{3/2} n^{ME}(S) dS$. Instead, for the new model with fractional moments, the volume fraction is directly calculate by $(1/\sqrt{6\pi})\mathrm{m}_{3/2}$. The results of the two computations are closely similar, and the L^1-norm difference relatively to the initial volume fraction field is less than 3% at $t = 1$. This validates the results of the new model. In fact, the EMSM model was compared with the Multi-fluid model in [38], and this comparison showed a high capacity of the EMSM model to predict the evaporation and the mean dynamics[4] of the spray.

7. Conclusions. In the present paper, we have proposed a new model for an evaporating polydisperse spray with the capacity of describing the interface geometry in the disperse phase, by analogy with the interface description in interfacial flows [19]. This model is a first step, in future work, toward a coupling with a diffuse interface model, where additional transport equation of geometrical variables will be used, in order to describe the atomization process with a unified model from the dense region to the polydisperse spray. However, this paper was not only dedicated to modeling issues, but also to tackle the different mathematical difficulties and to propose accurate and robust numerical schemes. Indeed, the new model involves a high order fractional size-moments, where the size is given by the droplet surface, which introduce a new mathematical framework and the need of adapted numerical schemes. The first issue is related to the size distribution closure with ME reconstruction. We have extended this continuous reconstruction in the case of integer moments [48, 47] to fractional moments. The second issue was related to the numerical scheme to solve the new model. For this purpose, we have used operator splitting techniques [17, 12] to separate the resolution of transport in the physical space and the source terms (evaporation and drag terms). The main difficulty with high order fractional moment

[4] Both the EMSM model and the present model, with one size-section, are limited in predicting the size-conditioned dynamics compared with Multi-fluid model because the Stokes number is computed with mean size. The extension of the EMSM model to CSVM model [64] tackles these issues.

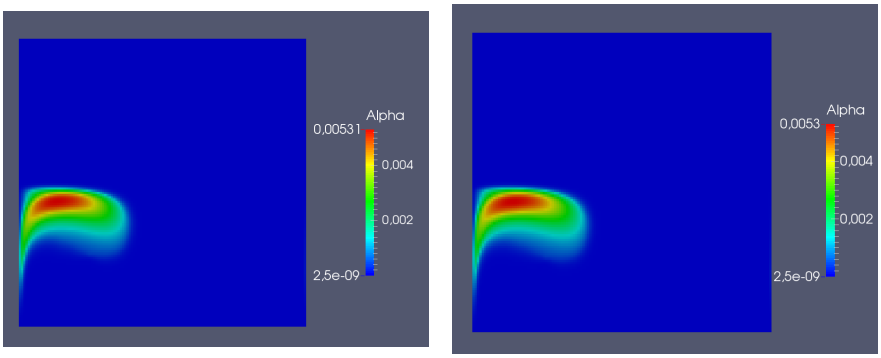

(a) EMSM (b) Fractional moments

Fig. 13: The spatial distribution of the volume fraction for the Taylor-Green simulation at $t = 0.5$. The computation is carried out in a uniform grid 128×128.

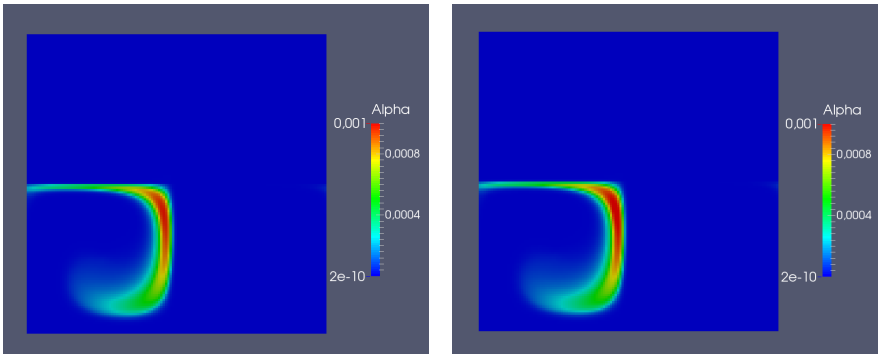

(a) EMSM (b) Fractional moments

Fig. 14: The spatial distribution of the volume fraction for the Taylor-Green simulation at $t = 1.0$. The computation is carried out in a uniform grid 128×128.

is to design accurate and realizable numerical scheme, especially for the resolution of the evaporation, where standard ODE solvers fail in ensuring these criteria. The proposed strategy consists in making the link with the kinetic evolution of the NDF for both transport in physical space and evaporation. For evaporation, we have found that the evolution of the moment of negative order are involved in the kinetic evolution of the evaporation, and we have seen how the proposed **NEMO** algorithm has improved the convergence and the accuracy of the solution. For transport resolution, we have extended the kinetic schemes developed in [38]. The proposed schemes are based on some moment theory [14], and we have extended some of these properties to fractional moments, in order to use this scheme in our case.

Furthermore, some extensions of the present numerical, especially evaporation, are straightforward and have been already discussed in this paper. We can also also

extend the model to the case of two-way coupling [23] and anisotropic Gaussian closure of the velocity distribution [63] for more accurate modeling of PTCs. However, the main challenge for the continuity of this work will be the modeling of the evolution of the averaging geometrical variables in the separated phases zone, where the key atomization mechanisms generating the polydisperse sprays are to be found.

Appendix A. Realistic droplet models. The closure models used in Section 2.1 are based on simplified assumptions. In this appendix, we demonstrate that the present contribution can be generalized to more realistic physical models. In this part, we consider a dilute spray of spherical droplets, where the droplets experience evaporation, drag and thermal transfer, and we neglect the collision, coalescence and fragmentation. In this context, WBE can be written as follows:

$$\partial_t f + \partial_{\boldsymbol{x}} \cdot (\boldsymbol{c} f) + \partial_{\boldsymbol{c}} \cdot (\boldsymbol{F} f) + \partial_S \left(\mathrm{R}_S f\right) + \partial_T \left(Q f\right) = 0, \tag{90}$$

Where the drag force $\boldsymbol{F}(t, \boldsymbol{x}, \boldsymbol{c}, S)$ depends on time, space, velocity and size. The evaporation rate $\mathrm{R}_S(t, \boldsymbol{x}, S, \boldsymbol{c}, T)$ and thermal transfer $Q(t, \boldsymbol{x}, S, \boldsymbol{c}, T)$ depend on the time, space, velocity, size and temperature.

We consider the following presumed NDF form:

$$f(t, \boldsymbol{x}, \boldsymbol{c}, T, S) = n(t, \boldsymbol{x}, S)\delta(\boldsymbol{c} - \boldsymbol{U}(t, \boldsymbol{x}, S))\delta(T - T_d(t, \boldsymbol{x}, S)) \tag{91}$$

The semi-kinetic equation can then be obtained by integrating (90) with respect to $(\boldsymbol{c}, T)$ after multiplying it by $(1, \boldsymbol{c}, e(T))^t$, where $e(T) = e_0 + \int_{T_0}^{T} C_{v,l}(T')\mathrm{d}T'$ and $C_{v,l}(T)$ is the liquid fuel heat capacity at constant volume:

$$\begin{array}{rcl} \partial_t n + \partial_{\boldsymbol{x}} \cdot (n\boldsymbol{U}) &=& \partial_S(\mathrm{R}_d n), \\ \partial_t n\boldsymbol{U} + \partial_{\boldsymbol{x}} \cdot (n\boldsymbol{U} \otimes \boldsymbol{U}) &=& \partial_S \left(n\mathrm{R}_d \boldsymbol{U}\right) + n\boldsymbol{F}_d \\ \partial_t n e_d + \partial_{\boldsymbol{x}} \cdot (n\boldsymbol{U} e_d) &=& \partial_S \left(n\mathrm{R}_d \boldsymbol{U}\right) + n C_{v,l}(T_d) Q_d. \end{array} \tag{92}$$

where $\mathrm{R}_d = \mathrm{R}_S(t, \boldsymbol{x}, \boldsymbol{U}, S, T_d)$, $Q_d = Q(t, \boldsymbol{x}, \boldsymbol{U}, S, T_d)$, $\boldsymbol{F}_d = \boldsymbol{F}(t, \boldsymbol{x}, \boldsymbol{U}_d, S)$ and $e_d = e(T_d)$.

In the following, we consider that the temperature and the velocity are independent of the droplet size. Then, we derive the moment governing equation from the semi-kinetic system:

$$\left\{ \begin{array}{ccccc} \partial_t \mathrm{m}_0 & + & \partial_{\boldsymbol{x}} \cdot (\mathrm{m}_0 \boldsymbol{U}) & = & -n\mathrm{R}_d|_{S=0}, \\ \partial_t \mathrm{m}_{1/2} & + & \partial_{\boldsymbol{x}} \cdot \left(\mathrm{m}_{1/2} \boldsymbol{U}\right) & = & G_{\mathrm{m}_{1/2}}, \\ \partial_t \mathrm{m}_1 & + & \partial_{\boldsymbol{x}} \cdot (\mathrm{m}_1 \boldsymbol{U}) & = & G_{\mathrm{m}_1}, \\ \partial_t \mathrm{m}_{3/2} & + & \partial_{\boldsymbol{x}} \cdot \left(\mathrm{m}_{3/2} \boldsymbol{U}\right) & = & G_{\mathrm{m}_{3/2}}, \\ \partial_t \left(\mathrm{m}_1 \boldsymbol{U}\right) & + & \partial_{\boldsymbol{x}} \cdot (\mathrm{m}_1 \boldsymbol{U} \otimes \boldsymbol{U}) & = & G_{\mathrm{m}_1 \boldsymbol{U}}, \\ \partial_t \left(\mathrm{m}_1 e_d\right) & + & \partial_{\boldsymbol{x}} \cdot (\mathrm{m}_1 \boldsymbol{U} e_d) & = & G_{\mathrm{m}_1 e_d}, \end{array} \right. \tag{93}$$

where the source terms are expressed as follows:

$$\begin{array}{rcl} G_{\mathrm{m}_{k/2}} &=& -\int_0^1 k/2 S^{k/2-1} \mathrm{R}_d(S) n(S) \mathrm{d}S \\ G_{\mathrm{m}_1 \boldsymbol{U}} &=& -\boldsymbol{U} \int_0^1 \mathrm{R}_d(S) n(S) \mathrm{d}S + \int_0^1 S \boldsymbol{F}_d(S) n(S) \mathrm{d}S \\ G_{\mathrm{m}_1 e_d} &=& -e_d \int_0^1 \mathrm{R}_d(S) n(S) \mathrm{d}S + C_{v,l}(T_d) \int_0^1 S Q_d(S) n(S) \mathrm{d}S \end{array} \tag{94}$$

The closure of the system is achieved by a continuous reconstruction through the maximization of Shannon Entropy.

We use the operator splitting technique to solve numerically the system (93). The transport part can be solved in the same way as it was done in section 5. In the following, we focus on the resolution of the source term part. Let us consider a spatial homogeneous domain, where only source terms are involved, the equation system becomes:

$$d_t \mathcal{M} = \mathcal{S}(t, \mathcal{M}) \tag{95}$$

where $\mathcal{M} = (\mathrm{m}_0, \mathrm{m}_{1/2}, \mathrm{m}_1, \mathrm{m}_{3/2}, \mathrm{m}_1 \boldsymbol{U}, \mathrm{m}_1 e_d)^T$ is the unknown vector and $\mathcal{S} = (-\mathrm{R}_d n^{ME}(\mathbf{m})|_{S=0}, G_{\mathrm{m}_0}, G_{\mathrm{m}_{1/2}}, G_{\mathrm{m}_1}, G_{\mathrm{m}_{3/2}}, G_{\mathrm{m}_1 \boldsymbol{U}}, G_{\mathrm{m}_1 e_d})^T$ is the source term. The four moments are computed by using **NEMO** algorithm with a slight adaptation in the fourth step, where the equation (73) is replaced by:

$$\mathrm{m}_{k/2}(t_n + \Delta t) = \sum_{j=1}^{n_q} w_j \widetilde{S}(t_n + \Delta t; t_n, S_j)^{k/2}, \tag{96}$$

where the weight w_j and abscissas S_j are determined in the third step of the algorithm and the $\widetilde{S}(t; t_0, s_0)$ is defined as follows:

$$\left\{ \begin{array}{rcl} \dfrac{d\widetilde{S}(t; t_0, s_0)}{dt} & = & \mathrm{R}_S(t, \widetilde{S}(t; t_0, s_0), \boldsymbol{U}, T_d), \\ \widetilde{S}(t_0; t_0, s_0) & = & s_0. \end{array} \right. \tag{97}$$

where the temperature T_d can be determined from the averaged internal energy e_d.

The updated velocity and the internal energy are computed using the CQMOM technique, as explained in Section 4.2. For $t \in [t_n, t_{n+1}]$, we write after subtracting the disappearance flux from the moments:

$$\begin{array}{rcl} (\mathrm{m}_1 \boldsymbol{U})^{[\widetilde{S}(t_n; t_{n+1}, 0), 1]}(t) & = & \displaystyle\sum_{i=1}^{n_q} w_i \widetilde{S}(t; t_n, S_i) \boldsymbol{c}_i(t) \\ (\mathrm{m}_1 e_d)^{[\widetilde{S}(t_n; t_{n+1}, 0), 1]}(t) & = & \displaystyle\sum_{i=1}^{n_q} w_i \widetilde{S}(t; t_n, S_i) e_i(t) \end{array} \tag{98}$$

with

$$\left\{ \begin{array}{rcl} \dfrac{d\boldsymbol{c}_i}{\Delta t} & = & \boldsymbol{F}(t, \widetilde{S}(t; t_n, S_i), \boldsymbol{c}_i) \\ \boldsymbol{c}_i(t = t_n) & = & \boldsymbol{U}(t_n), \end{array} \right. \tag{99}$$

and

$$\left\{ \begin{array}{rcl} \dfrac{de_i}{\Delta t} & = & Q(t, \widetilde{S}(t; t_n, S_i), \boldsymbol{c}_i, T_d) \\ e_i(t = t_n) & = & e_d(t_n), \end{array} \right. \tag{100}$$

We recall that the superscript $[\widetilde{S}(t_n; t_{n+1}, 0), 1]$ refers to the moments of the measure defined in the support $[\widetilde{S}(t_n; t_{n+1}, 0), 1]$, where $\widetilde{S}(t_n; t_{n+1}, 0)$ is the size of the last

evaporated droplet.

Appendix B. Fractional moment space. The purpose of this part is to extend some definition and relevant properties of the integer moment space to fractional moment space, in order to provide necessary tools to characterize the topology of this space, thus we can design realizable numerical schemes. In the following, we use the normalized fractional moments $\mathrm{c}_{k/2} = \mathrm{m}_{k/2}/\mathrm{m}_0$.

DEFINITION 7. *We define the the Nth fractional moment space as follows:*

$$\mathbb{M}_N^{1/2}([0,1]) = \{\mathbf{c}_N(\mu) \backslash \mu \in \mathrm{P}([0,1])\}\,,\ \mathbf{c}_N(\mu) = (\mathrm{c}_0(\mu), \mathrm{c}_{1/2}(\mu), \ldots, \mathrm{c}_{N/2}(\mu))^t,$$

where $\mathrm{P}([0,1])$ *denotes the set of probability density measures defined on the interval* $[0,1]$ *and* $\mathrm{c}_{k/2} = \int_0^1 x^{k/2} d\mu(x)$.

The fractional moments can be expressed as integer moment by using the following substitution $r^2 = x$:

$$\mathrm{c}_{k/2}(\mu) = \int_0^1 x^{k/2}\mu(x)dx = \int_0^1 r^k \underbrace{(2r\mu(r^2))}_{\widetilde{\mu}(r)} dr \tag{101}$$

This relation expresses an identification between the fractional moment $\mathrm{c}_{k/2}(\mu)$ of the measure μ and the integer moment $\widetilde{\mathrm{c}}_k = \mathrm{c}_k(\widetilde{\mu})$ of the measure $\widetilde{\mu}(r) = 2r\mu(r^2)$. In the following, we use these notations to differentiate between the two natures of the moments, even if they are equal. With this simple identification, we will take benefit from the already existed results of integer moment space to extend them to the case of fractional moment space.

For a fractional moment vector $\mathbf{c}_N \in \mathbb{M}_N^{1/2}([0,1])$, we denote by $\mathrm{P}_N(\mathbf{c}_N)$ the set of all measure $\mu \in \mathrm{P}([0,1])$, which are the solution of the following finite Hausdorff problem:

$$\mathrm{c}_{k/2} = \int_0^1 x^{k/2}\mu(x)dx, \quad k/2 \leq N/2 \tag{102}$$

If $\mathbf{c}_N = (\mathrm{c}_0, \ldots, \mathrm{c}_{N/2})^t$ belongs to the interior of $\mathbb{M}_N^{1/2}([0,1])$, we can show that the set $\mathrm{P}_N(\mathbf{c}_N)$ is infinite. Indeed, these results were shown in [14] for integer moments, and its generalization for fractional is straightforward through the identification (101). Furthermore, the set of $\mathrm{c}_{(N+1)/2}(\mu)$, where $\mu \in \mathrm{P}(\mathbf{c}_N)$, is infinite and

$$\mathrm{c}^-_{(N+1)/2}(\mathbf{c}_N) = \min_{\mu \in \mathrm{P}(\mathbf{c}_N)} \left\{\mathrm{c}_{(N+1)/2}(\mu)\right\}, \quad \mathrm{c}^+_{(N+1)/2}(\mathbf{c}_N) = \max_{\mu \in \mathrm{P}(\mathbf{c}_N} \left\{\mathrm{c}_{(N+1)/2}(\mu)\right\} \tag{103}$$

We define the canonical fractional moment as follows:

$$p_k = \frac{\mathrm{c}_{k/2} - \mathrm{c}^-_{k/2}(\mathbf{c}_k)}{\mathrm{c}^+_{k/2}(\mathbf{c}_k) - \mathrm{c}^-_{k/2}(\mathbf{c}_k)}. \tag{104}$$

The canonical moment vector belongs to $[0,1]^N$, which has a simple topology compared to the moment space. By using the results obtained on canonical integer moments [14], we can write the algebraic relation between fractional moments and their

corresponding canonical moments, in the case of $N = 3$, by using the identification (101):

$$p_1 = \frac{\mathrm{m}_{1/2}}{\mathrm{m}_0}, \quad p_2 = \frac{\mathrm{m}_0\mathrm{m}_1 - \mathrm{m}_{1/2}^2}{(\mathrm{m}_0 - \mathrm{m}_{1/2})\mathrm{m}_{1/2})}, \quad p_3 = \frac{(\mathrm{m}_0 - \mathrm{m}_{1/2})(\mathrm{m}_{1/2}\mathrm{m}_{3/2} - \mathrm{m}_1^2)}{(\mathrm{m}_0\mathrm{m}_1 - \mathrm{m}_{1/2}^2)(\mathrm{m}_{1/2} - \mathrm{m}_1)}. \tag{105}$$

If the moment vector $\mathbf{c}_N \in \mathbb{M}_N^{1/2}$, the vector $\mathbf{c}_{N+1}^{\pm} = (\mathrm{m}_0, \ldots, \mathrm{m}_{N/2}, \mathrm{c}_{(N+1)/2}^{\pm}(\mathbf{c}_N))$ belongs to the boundary of the moment space $\mathbb{M}_{N+1}^{1/2}$, and the measure set $\mathrm{P}_{N+1}(\mathbf{c}_{N+1}^{\pm}) = \{\mu_{\pm}\}$ has only one element. The measure μ_+ (resp μ_-) is called the upper (resp lower) principal representation. In the case of integer moment vector $\widetilde{\mathbf{c}}_N$, it was shown that the lower and upper principal representation ($\widetilde{\mu}_+$ and $\widetilde{\mu}_-$) can be expressed as sum of $n_s \leq (N+1)/2$ weighted delta-Dirac functions (we count the abscissas in the interior $]0,1[$ by 1 and the ones in the extremity (0 or 1) by 1/2) [14].

$$\widetilde{\mu}_{\pm}(r) = \sum_{i=1}^{n_s} \widetilde{w}_i^{\pm} \delta_{r_i^{\pm}}(r) \tag{106}$$

we recall that the subscript $\widetilde{\bullet}$ is used for integer moments and its corresponding measure, which are related to the fractional moments according to the identification (101). The Product-Difference (PD) algorithm [29] can be used to determine the weight and the abscissas of the low principal representation depending on the moment $\widetilde{\mathbf{c}}_N$. In other words, this algorithm solve the following non-linear system:

$$\widetilde{\mathrm{c}}_k = \sum_{i=1}^{n_s} \widetilde{w}_i^{-} r_-^k, \quad k = 0, 1, \ldots, N \tag{107}$$

The identification (101) allow us to relate the the lower principal representation μ_- in terms of fractional moments, to the lower principal representation $\widetilde{\mu}_-$ in terms of integer moments as follows:

$$\mu_-(x) \quad = \quad \frac{1}{2\sqrt{x}} \widetilde{\mu}_-(\sqrt{x}), \tag{108}$$

PROPOSITION 8. *Let r be a positive real number, then for all positive real x we have:*

$$\frac{\delta_r(\sqrt{x})}{2\sqrt{x}} = \delta_{r^2}(x). \tag{109}$$

Proof. Let f be an integrable function in $L_1([0,1])$:

$$\begin{array}{rcl} \int_0^{+\infty} \frac{\delta_r(\sqrt{x})}{2\sqrt{x}} f(x)dx & \underbrace{=}_{y=\sqrt{x}} & \int_0^{+\infty} \delta_r(y) f(y^2) dy \\ & = & f(r^2). \end{array} \tag{110}$$

Hence the result. ∎

Using the last proposition, we deduce that:

$$\mu_-(x) = \sum_{i=1}^{n_s} w_i^{-} \delta_{x_i^{-}}(x), \tag{111}$$

where $x_i^- = (r_i^-)^2$ and $w_i^- = \tilde{w}_i^-$.
Thus, we can reused the PD algorithm to determine the weights and abscissas of the lower principal representation for fractional moment.

Appendix C. Transport scheme. In this part, we present a first and a second order scheme, which are derived from the kinetic approach present in 5.

C.1. First order scheme. For a first order scheme, we consider a constant piecewise reconstruction for the moments and the velocity. Then the fluxes become:

$$\begin{pmatrix} F_{i+1/2} \\ G_{i+1/2} \end{pmatrix} = \begin{pmatrix} m_{0,i}^n \\ m_{1/2,i}^n \\ m_{1,i}^n \\ m_{3/2,i}^n \\ m_{1,i}^n u_{0,i}^n \\ m_{1,i}^n v_i^n \end{pmatrix} max(u_i^n, 0) + \begin{pmatrix} m_{0,i+1}^n \\ m_{1/2,i+1}^n \\ m_{1,i+1}^n \\ m_{3/2,i+1}^n \\ m_{1,i+1}^n u_{0,i+1}^n \\ m_{1,i}^n v_{i+1}^n \end{pmatrix} min(u_{i+1}^n, 0), \tag{112}$$

C.2. Second order scheme. Kah et al [38] developed a realizable second order kinetic scheme. They showed that the canonical moments (in the context of integer moments) are transported variables. Therefore, these quantities satisfy a maximum principle. Since, the canonical moments live in the simple space $[0,1]^N$ ($N = 3$ in our case). The authors proposed to use linear reconstruction of the canonical moments to design a high order scheme, instead of reconstructing directly the moments, which belong to a complex space. We adopt the same approach with some adaptations for the fractional moments. After reconstructing the variables (velocity and canonical moments) the fluxes are computed by a simple integration.

C.2.1. Reconstruction. The reconstructed variables are the moment m_0, the canonical moments (defined in the appendix B) p_1, p_2, p_3 and the velocity.

$$\left\{ \begin{array}{rcl} \mathrm{m}_0(x) & = & \mathrm{m}_{0,i} + Dm_{0,i}(x - x_i), \\ p_1(x) & = & \overline{p_{1,i}} + Dp_{1,i}(x - x_i), \\ p_2(x) & = & \overline{p_{2,i}} + Dp_{2,i}(x - x_i), \\ p_3(x) & = & \overline{p_{3,i}} + Dp_{3,i}(x - x_i), \\ u(x) & = & \overline{u_i} + Du_i(x - x_i), \\ v(x) & = & \overline{v_i} + Dv_i(x - x_i), \end{array} \right. \tag{113}$$

where $x \in [x_{i-1/2}, x_{i+1/2}]$. Generally the quantities with the bar are different from the cell averaged quantities $p_{k,i}$, $u_{k,i}$ and $v_{k,i}$ and they are determined depending on the slopes and the following conservation properties:

(114)

$$\begin{array}{rcl} \mathrm{m}_{1/2,i}^n & = & \frac{1}{\Delta x} \int_{x_{i-1/2}}^{x_{i+1/2}} \mathrm{m}_0(x) p_1(x) dx, \\ \mathrm{m}_{1,i}^n & = & \frac{1}{\Delta x} \int_{x_{i-1/2}}^{x_{i+1/2}} \mathrm{m}_0(x) p_1(x) [(1-p_1)p_2 + p_1](x) dx, \\ \mathrm{m}_{3/2,i}^n & = & \frac{1}{\Delta x} \int_{x_{i-1/2}}^{x_{i+1/2}} \mathrm{m}_0 p_1 \left\{ (1-p_1)(1-p_2)p_2 p_3 + [(1-p_1)p_2 + p_1]^2 \right\}(x) dx, \\ m_{1,i}^n u_i^n & = & \frac{1}{\Delta x} \int_{x_{i-1/2}}^{x_{i+1/2}} \mathrm{m}_0(x) p_1(x) [(1-p_1)p_2 + p_1](x) u(x) dx. \end{array}$$

Compared to the expressions developed in the case of the EMSM model, only the last integral expression is different. In fact, the velocity is weighted with the moment m_1

for both models, but in the new model, m_1 seems as a second order moment. For this reason, the expression of the moment m_1 as function of the canonical moment is different from the one in the case of integer moments.

Kah el al. [38] show that the bar terms can be written as follows:

$$\begin{aligned} \overline{p_{k,i}} &= a_{k,i} + b_{k,i} Dp_{k,i}, \\ \overline{u_i} &= a_{u,i} + b_{u,i} Du_i, \end{aligned} \tag{115}$$

where for each k, $a_{k,i}$ and $b_{k,i}$ are independent of $Dp_{k,i}$, and $a_{u,i}$ and $b_{u,i}$ are independent of Du_i.

C.2.2. Slope limitation. In order to satisfy the maximum principle for the transported quantities (the canonical moment and the velocity) and the positivity of the number density m_0, the slopes should be calculated carefully. Following the development done in [38], the slopes are calculated as follows:

$$\begin{aligned} Dm_{0,i} &= \phi(\mathrm{m}^n_{0,i-1}, \mathrm{m}^n_{0,i}, \mathrm{m}^n_{0,i}) \min\left(\frac{|\mathrm{m}^n_{0,i+1} - \mathrm{m}^n_{0,i}|}{\Delta x}, \frac{|\mathrm{m}^n_{0,i} - \mathrm{m}^n_{0,i-1}|}{\Delta x}, \frac{2\mathrm{m}^n_{0,i}}{\Delta x} \right), \\ Dp_{k,i} &= \phi(p^n_{k,i-1}, p^n_{k,i}, p^n_{k,i+1}) \min\left(\frac{|p^n_{k,i+1} - a_{k,i}|}{\Delta x + 2b_{k,i}}, \frac{|a_{k,i} - p^n_{k,i-1}|}{\Delta x - 2b_{k,i}} \right), \\ Du_i &= \phi(u^n_{i-1}, u^n_i, u^n_{i+1}) \min\left(\frac{|u^n_{i+1} - u^n_i|}{\Delta x + 2b_{u,i}}, \frac{|u^n_i - u^n_{i-1}|}{\Delta x - 2b_{u,i}}, \frac{1}{\Delta t} \right), \end{aligned} \tag{116}$$

where $\phi(a,b,c) = 1/2(sgn(b-a) + sgn(c-b))$.

Using the equations (114),(115) and (116) the slopes and the bar variables can be expressed as function of the current and neighbor cell variables. However, these algebra relations are quite heavy. Therefore, its calculation is achieved using Maple software.

C.2.3. Fluxes Computation. After computing the slopes and the bar variables, the fluxes can be computed as follows:

$$\begin{pmatrix} F^+_{i+1/2} \\ G^+_{i+1/2} \end{pmatrix} = \frac{1}{\Delta t} \int_{x^L_{i+1/2}}^{x_{i+1/2}} \mathrm{m}_0 \begin{pmatrix} 1 \\ p_1 \\ p_1[(1-p_1)p_2 + p_1] \\ p_1\left\{(1-p_1)(1-p_2)p_2p_3 + [(1-p_1)p_2 + p_1]^2\right\} \\ p_1[(1-p_1)p_2 + p_1]u \\ p_1[(1-p_1)p_2 + p_1]v \end{pmatrix} dx, \tag{117}$$

and

$$\begin{pmatrix} F^-_{i+1/2} \\ G^-_{i+1/2} \end{pmatrix} = -\frac{1}{\Delta t} \int_{x_{i+1/2}}^{x^R_{i+1/2}} \mathrm{m}_0 \begin{pmatrix} 1 \\ p_1 \\ p_1[(1-p_1)p_2 + p_1] \\ p_1\left\{(1-p_1)(1-p_2)p_2p_3 + [(1-p_1)p_2 + p_1]^2\right\} \\ p_1[(1-p_1)p_2 + p_1]u \\ p_1[(1-p_1)p_2 + p_1]v \end{pmatrix} dx, \tag{118}$$

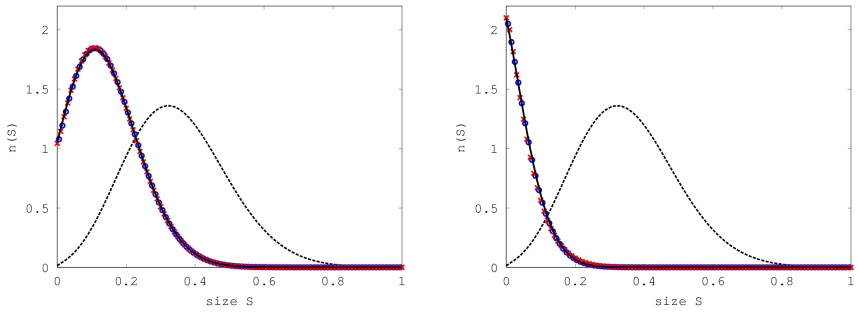

(a) t=0.3 (b) t=0.6

Fig. 15: The evolution of the NDF in the case of a linear evaporation rate: initial ME reconstructed solution (dashed line), **NEMO** algorithm using $n_q^- = 1$ (cross), fully kinetic algorithm (circle) and exact kinetic solution (solid line), at times $t = 0.3$ and $t = 0.6$.

such that

$$
\begin{aligned}
x^L_{i+1/2} &= x_{i+1/2} - \Delta t \frac{(\bar{u}_i + \frac{\Delta x}{2} D u_i)_+}{1 + \Delta t D u_i}, \\
x^R_{i+1/2} &= x_{i+1/2} - \Delta t \frac{(\bar{u}_{i+1} - \frac{\Delta x}{2} D u_{i+1})_+}{1 + \Delta t D u_{i+1}}.
\end{aligned} \tag{119}
$$

The expression inside the integrals are polynomial functions of x of order up to 6, its calculation can be achieved by using three points of the Gauss-Legendre quadrature.

Appendix D. Accuracy of NEMO algorithm for non constant evaporation laws. **NEMO** scheme has been developed under the assumption of a d^2 law, but as it was explained before, the algorithm can be generalized for more complex law by solving the Lagrangian equation (49) for each abscissas S_j given in the third step of the algorithm. In this section, we propose to evaluate the accuracy of the algorithm in the case where the evaporation rate depends linearly on the size:

$$
R_s(S) = -(a + bS). \tag{120}
$$

The exact kinetic solution can be computed according to the equation (51). In the following, we set $a = 0.5$ and $b = 1$. Figure 15 present the NDFs computed by **NEMO** algorithm, fully kinetic algorithm and compared to the exact solution at $t = 0.3$ and $t = 0.6$. And the relative error are given in Figure 16. We can see from these results, the accuracy of the generalized **NEMO** algorithm to predict the kinetic evolution.

Acknowledgments. This research was supported by a Ph.D. grant for Mohamed Essadki from IFP Energies nouvelles and EM2C. We would like to thank Adam Larat and Aymeric Vié for several interesting and helpful discussions. The helpful comments of Thibaut Ménard are also gratefully acknowledged.

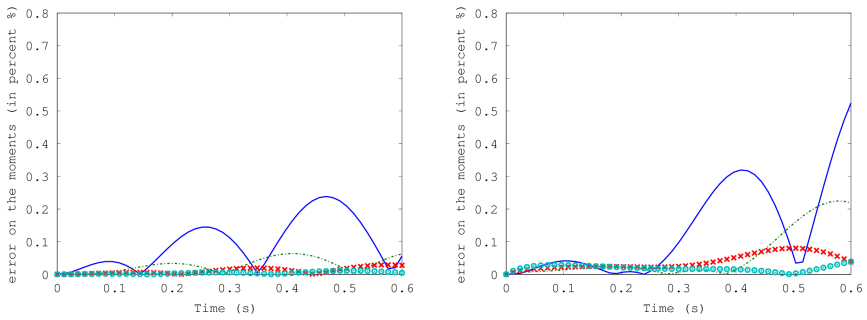

(a) fully kinetic algorithm (b) **NEMO** algorithm with $n_q^- = 1$

Fig. 16: Evolution of the moment errors relatively to their initial value calculated with fully kinetic algorithm (left) and **NEMO** algorithm (right): m_0 (solid line), $m_{1/2}$ (Dash-dotted line), m_1 (cross) and $m_{3/2}$ (circle).

REFERENCES

[1] M. Arienti and M. Sussman, *An embedded level set method for sharp-interface multiphase simulations of Diesel injectors*, International Journal of Multiphase Flow, 59 (2014), pp. 1–14.

[2] M. R. Baer and J. W. Nunziato, *A two-phase mixture theory for the deflagration-to-detonation transition (DDT) in reactive granular materials*, International Journal of Multiphase Flow, 12 (1986), pp. 861–889.

[3] G. A. Bird, *Molecular gas dynamics and the direct simulation of gas flows*, Oxford Science Publications, 42 (1994).

[4] M. Boileau, C. Chalons, J.-F. Bourgouin, C. Terrier, and F. Laurent, *Robust numerical schemes for eulerian spray DNS and LES in two-phase turbulent flows*, in International Conference on Multiphase Flow, 2010, pp. 1–15.

[5] M. Boileau, C. Chalons, and M. Massot, *Robust numerical coupling of pressure and pressureless gas dynamics equations for Eulerian spray DNS and LES*, SIAM J. Sci. Comput., 37 (2015), pp. B79–B102.

[6] F. Bouchut, S. Jin, and X. Li, *Numerical approximations of pressureless and isothermal gas dynamics*, SIAM J. Num. Anal., 41 (2003), pp. 135–158.

[7] G. Bruneaux, *Mixing process in high pressure diesel jets by normalized laser induced exciplex fluorescence part i: Free jet*, SAE Technical Paper, 114 (2005), pp. 1444–1461.

[8] C. Burstedde, L. C. Wilcox, and O. Ghattas, *p4est: Scalable algorithms for parallel adaptive mesh refinement on forests of octrees*, SIAM Journal on Scientific Computing, 33 (2011), pp. 1103–1133.

[9] V. L. Chenadec and H. Pitsch, *A 3D unsplit forward/backward volume-of-fluid approach and coupling to the level set method*, Journal of Computational Physics, 233 (2013), pp. 10 – 33.

[10] S. de Chaisemartin, *Eulerian models and numerical simulation of turbulent dispersion for polydisperse evaporation sprays*, PhD thesis, Ecole Centrale Paris, France, 2009. Available on TEL : http://tel.archives-ouvertes.fr/tel-00443982/en/.

[11] S. de Chaisemartin, L. Fréret, D. Kah, F. Laurent, R. Fox, J. Reveillon, and M. Massot, *Eulerian models for turbulent spray combustion with polydispersity and droplet crossing*, Comptes Rendus Mécanique, 337 (2009), pp. 438–448. Special Issue 'Combustion for Aerospace Propulsion'.

[12] S. Descombes, M. Duarte, T. Dumont, F. Laurent, V. Louvet, and M. Massot, *Analysis of operator splitting in the non-asymptotic regime for nonlinear reaction-diffusion equations. application to the dynamics of premixed flames*, SIAM J. Numerical Analysis, 52 (2014), pp. 1311–1334.

[13] O. Desjardins, J. McCaslin, M. Owkes, and P. Brady, *Direct numerical and large-eddy simulation of primary atomization in complex geometries*, Atomization and Sprays, 23

(2013), pp. 1001–1048.
[14] H. Dette and W. J. Studden, *The theory of canonical moments with applications in statistics, probability, and analysis*, John Wiley & Sons Inc., New York, 1997.
[15] F. Doisneau, *Eulerian modeling and simulation of polydisperse moderately dense coalescing spray flows with nanometric-to-inertial droplets: application to Solid Rocket Motors*, PhD thesis, Ecole Centrale Paris, 2013. Available at http://tel.archives-ouvertes.fr/tel-00966185.
[16] F. Doisneau, F. Laurent, A. Murrone, J. Dupays, and M. Massot, *Eulerian multi-fluid models for the simulation of dynamics and coalescence of particles in solid propellant combustion*, J. Comp. Phys., 234 (2013), pp. 230–262.
[17] F. Doisneau, A. Sibra, J. Dupays, A. Murrone, F. Laurent, and M. Massot, *Numerical strategy for unsteady two-way coupled polydisperse sprays: application to solid-rocket instabilities*, Journal of Propulsion and Power, 3 (2014), pp. 727–748.
[18] D. Drew and S. Passman, *Theory of multicomponent fluids*, vol. 135, Springer, 1999.
[19] D. A. Drew, *Evolution of geometric statistics*, SIAM J. Appl. Math., 50 (1990), p. 649666.
[20] F. Drui, A. Fikl, P. Kestener, S. Kokh, A. Larat, V. Le Chenadec, and M. Massot, *Experimenting with the p4est library for AMR simulations of two-phase flows*, ESAIM : Proceedings and Surveys, 53 (2016), pp. 232–247.
[21] F. Drui, S. Kokh, A. Larat, and M. Massot, *A hierarchy of simple hyperbolic two-fluid models for bubbly flows*, submitted, (2016), pp. 1–23. available on HAL, https://hal.archives-ouvertes.fr/hal-01349441.
[22] C. Dumouchel, *Measurement of breakup length of cylindrical liquid jets. application to low-pressure car injector*, Atomization and Sprays, 11 (2001), pp. 201–226.
[23] O. Emre, *Modeling of spray polydispersion with two-way turbulent interactions for high pressure direct injection in engines*, PhD thesis, Ecole Centrale Paris, 2014. Available on TEL https://tel.archives-ouvertes.fr/tel-01089937.
[24] O. Emre, D. Kah, S. Jay, Q.-H. Tran, A. Velghe, S. De Chaisemartin, F. Laurent, and M. Massot, *Eulerian Moment Methods for Automotive Sprays*, Atomization and Sprays, 25 (2015), pp. 189–254.
[25] M. Essadki, S. de Chaisemartin, M. Massot, F. Laurent, A. Larat, and S. Jay, *High order moment methods and adaptive mesh refinement for polydisperse evaporating spray simulations*, Oil & Gas Science and Technology, (2016), pp. 1–25. In press, doi:10.2516/ogst/2016012.
[26] M. Frenklach, *Method of moments with interpolative closure*, Chemical Engineering Science, 57 (2002), pp. 2229–2239.
[27] M. Frenklach and S. J. Harris, *Aerosol dynamics modeling using the method of moments*, Journal of Colloid and Interface Science, 118 (1986), pp. 252–261.
[28] W. Gautschi, *Orthogonal polynomials computation and approximation*, Numerical mathematics and scientific computation, Oxford university press, Oxford, New York, Auckland, 2004.
[29] R. Gordon, *Error bounds in equilibrium statistical mechanics*, Journal of Mathematical Physics, 9 (1968), pp. 655–663.
[30] J. Greenberg, I. Silverman, and Y. Tambour, *On the origin of spray sectional conservation equations*, Combustion and Flame, 93 (1993), pp. 90–96.
[31] H. Gzyl and A. Tagliani, *Hausdorff moment problem and fractional moments*, Appl. Math. Comput., 216 (2010), pp. 3319–3328.
[32] F. Harlow and J. E. Welch, *Numerical calculation of time-dependent viscous incompressible flow of fluid with free surface*, Physics of Fluids, 8 (1965), pp. 2182–2189.
[33] C. Hirt, A. Amsden, and J. Cook, *An arbitrary lagrangian-eulerian computing method for all flow speeds*, Journal of Computational Physics, 14 (1974), pp. 227–253.
[34] L. Itani, G. Bruneaux, A. D. Lella, and C. Schulz, *Two-tracer {LIF} imaging of preferential evaporation of multi-component gasoline fuel sprays under engine conditions*, Proceedings of the Combustion Institute, 35 (2015), pp. 2915 – 2922.
[35] S. Jay, F. Lacas, and S. Candel, *Combined surface density concepts for dense spray combustion*, Combustion and Flame, 144 (2006), pp. 558–577.
[36] D. Kah, *Taking into account polydispersity in the framework of a coupled Euler-Lagrange approach for the modeling of liquid fuel injection in internal combustion engines*, PhD thesis, Ecole Centrale de Paris, 2010. available online at http://tel.archives-ouvertes.fr/tel-00618786/en/.
[37] D. Kah, O. Emre, Q. Tran, S. de Chaisemartin, S. Jay, F. Laurent, and M. Massot, *High order moment method for polydisperse evaporating spray with mesh movement: application to internal combustion engines*, International Journal of Multiphase Flows, 71 (2015), pp. 38–65.

[38] D. Kah, F. Laurent, M. Massot, and S. Jay, *A high order moment method simulating evaporation and advection of a polydisperse spray*, Journal of Computational Physics, 231 (2012), pp. 394–422.
[39] J. N. Kapur and H. K. Kesavan, *Entropy optimization principles with applications*, Academic Press, Inc., Boston, MA, 1992.
[40] M. L. M., B. G., M. Meijer, and E. J., *Characterization of a set of ecn spray a injectors: Nozzle to nozzle variations and effect on spray characteristics*, SAE International Journal of Engines, 114 (2013), pp. 24–37.
[41] F. Laurent and M. Massot, *Multi-fluid modeling of laminar poly-dispersed spray flames: origin, assumptions and comparison of the sectional and sampling methods*, Combust. Theory and Modelling, 5 (2001), pp. 537–572.
[42] F. Laurent, M. Massot, and P. Villedieu, *Eulerian multi-fluid modeling for the numerical simulation of coalescence in polydisperse dense liquid sprays*, Journal of Computational Physics, 194 (2004), pp. 505–543.
[43] F. Laurent, A. Sibra, and F. Doisneau, *Two-size moment Eulerian multi-fluid model: a robust and high-fidelity description of polydisperse moderately dense evaporating sprays*, Communications in Computational Physics, (2016), pp. 1–41. Accepted, available on HAL https://hal.archives-ouvertes.fr/hal-01169730.
[44] S. Le Martelot, R. Saurel, and B. Nkonga, *Towards the direct numerical simulation of nucleate boiling flows*, International Journal of Multiphase Flow, 66 (2014), pp. 62–78.
[45] C. Le Touze, *Coupling between separated and dispersed two-phase flow models for the simulation of primary atomization in cryogenic combustion*, PhD thesis, Universite Nice Sophia Antipolis, Dec. 2015. Available on TEL https://tel.archives-ouvertes.fr/tel-01250527.
[46] R. Lebas, T. Menard, P. A. Beau, A. Berlemont, and F. X. Demoulin, *Numerical simulation of primary break-up and atomization: DNS and modelling study*, Int. J. Multiphase Flows, 35 (2009), pp. 247–260.
[47] M. Massot, F. Laurent, D. Kah, and S. de Chaisemartin, *A robust moment method for evaluation of the disappearance rate of evaporating sprays*, SIAM J. Appl. Math., 70 (2010), pp. 3203–3234.
[48] L. R. Mead and N. Papanicolaou, *Maximum entropy in the problem of moments*, J. Math. Phys., 25 (1984), pp. 2404–2417.
[49] T. Menard, S. Tanguy, and A. Berlemont, *Coupling level set/VOF/ghost fluid methods: Validation and application to 3D simulation of the primary break-up of a liquid jet*, International Journal of Multiphase Flow, 33 (2007), pp. 510–524.
[50] M. E. Mueller, G. Blanquart, and H. Pitsh, *Hybrid method of moments for modeling soot formation and growth*, Combustion and Flame, 156 (2009), pp. 1143–1155.
[51] T. T. Nguyen, F. Laurent, R. O. Fox, and M. Massot, *Solution of population balance equations in applications with fine particles: mathematical modeling and numerical schemes*, Journal of Computational Physics, (2016), pp. 1–42. submitted, available on HAL https://hal.archives-ouvertes.fr/hal-01247390.
[52] P. Novi Inverardi, G. Pontuale, A. Petri, and A. Tagliani, *Hausdorff moment problem via fractional moments*, Appl. Math. Comput., 144 (2003), pp. 61–74.
[53] J. O'Connor, M. P. Musculus, and L. M. Pickett, *Effect of post injections on mixture preparation and unburned hydrocarbon emissions in a heavy-duty diesel engine*, Combustion and Flame, 170 (2016), pp. 111 – 123.
[54] L. Pickett, G. Bruneaux, and R. Payri, *Engine combustion network*, tech. report, Sandia National Laboratories, 2014. http://www.ca.sandia.gov/ecn.
[55] M. Sabat, *Eulerian modeling and numerical methods for the description of turbulent polydisperse sprays*, PhD thesis, Université Paris-Saclay, CentraleSuplec, 2016.
[56] R. Saurel and R. Abgrall, *A multiphase godunov method for compressible multifluid and multiphase flows*, Journal of Computational Physics, 150 (1999), pp. 425 – 467.
[57] R. Saurel, F. Petitpas, and R. A. Berry, *Simple and efficient relaxation methods for interfaces separating compressible fluids, cavitating flows and shocks in multiphase mixtures*, Journal of Computational Physics, 228 (2009), pp. 1678–1712.
[58] J. Shinjo and A. Umemura, *Simulation of liquid jet primary breakup: Dynamics of ligament and droplet formation*, International Journal of Multiphase Flow, 36 (2010), pp. 513 – 532.
[59] J. Shinjo and A. Umemura, *Surface instability and primary atomization characteristics of straight liquid jet sprays*, International Journal of Multiphase Flow, 37 (2011), pp. 1294 – 1304.
[60] S. A. Skeen, J. Manin, and L. M. Pickett, *Simultaneous formaldehyde {PLIF} and high-speed schlieren imaging for ignition visualization in high-pressure spray flames*, Proceedings of the Combustion Institute, 35 (2015), pp. 3167 – 3174.

[61] G. Talenti, *Recovering a function from a finite number of moments*, Inverse Problems, 3 (1987), pp. 501–517.
[62] A. Vallet, A. Burluka, and R. Borghi, *Development of a eulerian model for the "atomization" of a liquid jet*, Atomization and Sprays, 11 (2001), pp. 619–642.
[63] A. Vié, F. Doisneau, and M. Massot, *On the Anisotropic Gaussian closure for the prediction of inertial-particle laden flows*, Communication in Computational Physics, 17 (2015), pp. 1–46.
[64] A. Vié, F. Laurent, and M. Massot, *Size-velocity correlations in high order moment methods for polydisperse evaporating sprays: modeling and numerical issues*, J. Comp. Phys., 237 (2013), pp. 277–310.
[65] F. Williams, *Spray combustion and atomization*, Physics of Fluids, 1 (1958), pp. 541–545.
[66] C. Yuan, F. Laurent, and R. Fox, *An extended quadrature method of moments for population balance equations*, Atomization and Sprays, 51 (2012), pp. 1–23.
[67] B. Zhao, Z. Yang, M. V. Johnston, H. Wang, A. S. Wexler, and M. Balthasar, *Measurement and numerical simulation of soot particle size distribution functions in a laminar premixed ethylene-oxygen-argon flame*, Combustion and Flame, 133 (2003), pp. 173–188.